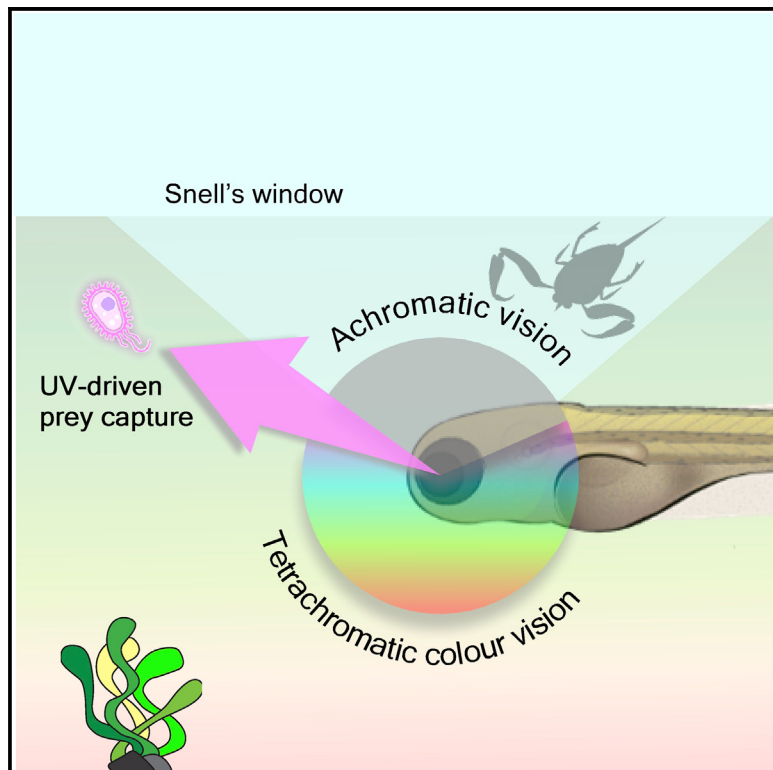


# Zebrafish Differentially Process Color across Visual Space to Match Natural Scenes

## Graphical Abstract



## Authors

Maxime J.Y. Zimmermann,  
Noora E. Nevala, Takeshi Yoshimatsu,  
Daniel Osorio, Dan-Eric Nilsson,  
Philipp Berens, Tom Baden

## Correspondence

t.baden@sussex.ac.uk

## In Brief

With half of their brain located inside the eyes, every neuron counts in the larval zebrafish retina. By 2-photon and hyperspectral natural imaging, Zimmermann et al. show how their near-360° visual field is functionally divided into tetrachromatic, achromatic, and UV prey-capture regions to match available visual information in nature.

## Highlights

- The larval zebrafish retina is anatomically and functionally asymmetric
- The upper-frontal visual field is dominated by UV-sensitive prey-capture circuits
- Circuits for tetrachromatic color vision survey the horizon and lower visual field
- This organization matches natural chromatic statistics and behavioral demands



# Zebrafish Differentially Process Color across Visual Space to Match Natural Scenes

Maxime J.Y. Zimmermann,<sup>1,6</sup> Noora E. Nevala,<sup>1,6</sup> Takeshi Yoshimatsu,<sup>1,6</sup> Daniel Osorio,<sup>1</sup> Dan-Eric Nilsson,<sup>2</sup> Philipp Berens,<sup>3,4,5</sup> and Tom Baden<sup>1,3,7,\*</sup>

<sup>1</sup>School of Life Sciences, University of Sussex, Brighton BN1 9QG, UK

<sup>2</sup>Lund Vision Group, University of Lund, 22362 Lund, Sweden

<sup>3</sup>Institute of Ophthalmic Research, University of Tübingen, 72076 Tübingen, Germany

<sup>4</sup>Bernstein Centre for Computational Neuroscience, University of Tübingen, 72076 Tübingen, Germany

<sup>5</sup>Centre for Integrative Neuroscience, University of Tübingen, 72076 Tübingen, Germany

<sup>6</sup>These authors contributed equally

<sup>7</sup>Lead Contact

\*Correspondence: [t.baden@sussex.ac.uk](mailto:t.baden@sussex.ac.uk)

<https://doi.org/10.1016/j.cub.2018.04.075>

## SUMMARY

Animal eyes have evolved to process behaviorally important visual information, but how retinas deal with statistical asymmetries in visual space remains poorly understood. Using hyperspectral imaging in the field, *in vivo* 2-photon imaging of retinal neurons, and anatomy, here we show that larval zebrafish use a highly anisotropic retina to asymmetrically survey their natural visual world. First, different neurons dominate different parts of the eye and are linked to a systematic shift in inner retinal function: above the animal, there is little color in nature, and retinal circuits are largely achromatic. Conversely, the lower visual field and horizon are color rich and are predominately surveyed by chromatic and color-opponent circuits that are spectrally matched to the dominant chromatic axes in nature. Second, in the horizontal and lower visual field, bipolar cell terminals encoding achromatic and color-opponent visual features are systematically arranged into distinct layers of the inner retina. Third, above the frontal horizon, a high-gain UV system piggybacks onto retinal circuits, likely to support prey capture.

## INTRODUCTION

Sensory systems have evolved to serve animals' behavioral requirements. They are tuned to prioritize behaviorally important computations subject to constraints on the neural hardware and metabolic cost [1, 2]. In vision, specializations are often made according to the statistics of specific regions in visual space. For example, mouse cones preferentially process dark contrasts above, but not below, the visual horizon, likely boosting the detection of aerial predators [3, 4]. However, beyond anisotropic receptor distributions, systematically linking the statistics of the visual world to the properties of visual systems has been difficult [5–8] (here, "anisotropy" is used to surmise any systematic asymmetry in anatomy or function with retinal

position). Making a link of this kind ideally requires an animal model that allows *in vivo* measurements of light-driven neuronal activity in any part of the eye. In addition, it is necessary to measure the visual characteristics of the animal's natural world and focus on aspects that are behaviorally important yet sufficiently low dimensional to be amenable to statistical evaluation. One model that meets these criteria is the color vision system of the larval zebrafish.

Within three days of hatching, larval zebrafish become highly visual animals with tetrachromatic wide-angle vision [9, 10] and well-studied visual behaviors [11–16]. Vision is metabolically costly for larval zebrafish: the two eyes make up nearly a quarter of the total body volume, with the neuronal retina taking up >75% of each eye. Indeed, about half of the larva's central neurons are located inside the eyes (STAR Methods). Space limitations and energy demand create strong evolutionary pressure to make the best use of every visual neuron—potentially driving regional specializations within the eye. Here, we examine how larval zebrafish retinal circuits process chromatic information in the immediate context of their natural visual world and their behavioral demands. Throughout, we used zebrafish larvae at 7 or 8 days post-fertilization (dpf) (for discussion on the choice of age, see STAR Methods). We find that the eye is functionally and anatomically extremely anisotropic, and these anisotropies match an asymmetrical distribution of chromatic content in the zebrafish natural habitat.

## RESULTS

### Chromatic Content in Nature Varies with Visual Elevation

Zebrafish are surface-dwelling freshwater fish of the Indian sub-continent [17, 18]. Larval and juvenile zebrafish live mostly in shallow, low-current pockets on the sides of streams and rice paddies—probably to avoid predation by larger fish [19], to conserve energy and to facilitate visually guided prey capture of aquatic micro-organisms, such as paramecia [11, 13, 15]. To systematically record how the visual world varies with elevation in the zebrafish natural habitat, we used two complementary approaches: (1) an action camera to take underwater 180° wide-angle, high-spatial-resolution photographs (Figures 1A–1E)



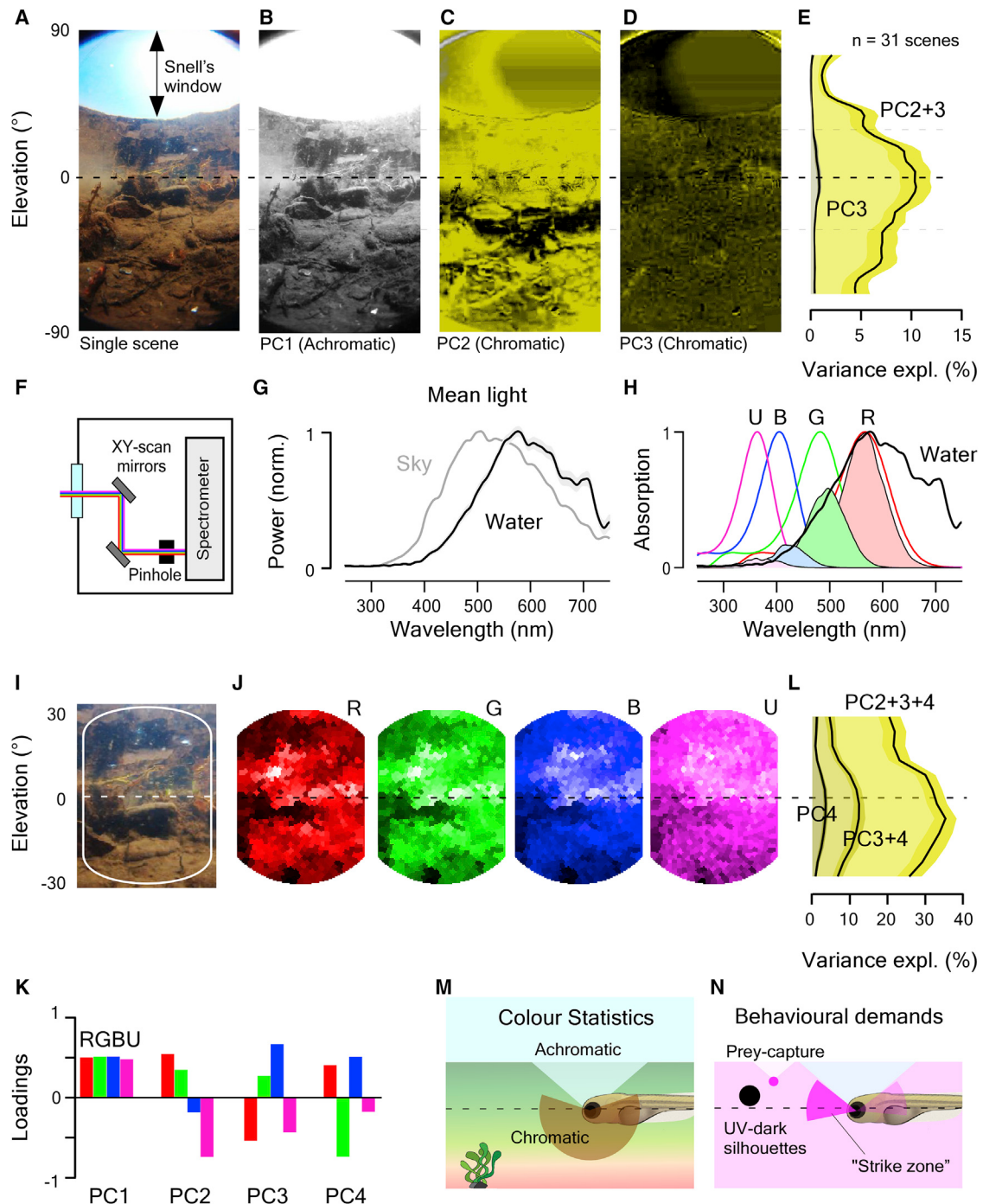


**Figure 1. Distribution of Chromatic Content in the Zebrafish Natural Visual World**

(A) Example 180° underwater photograph taken in zebrafish-inhabited waters in West Bengal, India.

(B–D) The first three principal components across the chromatic dimension (R, G, and B) of the image in (A). PC1 (B) reflects the achromatic image content, whereas PCs 2 (C) and 3 (D; false color coded in shades of yellow) reflect the remaining chromatic content.

(E) Variance explained by PC3 and PC2+3 across all 31 images calculated from 5° horizontal images slices. Error shadings are in SD.

(F) Schematic of the custom-built hyperspectral scanner. X and Y mirrors are moved through 1,000 regularly spaced positions over a 60° circular window to deflect a ~2.8° spot of light into a spectrometer and thereby build up a hyperspectral image [3, 20].

(G) Mean of n = 31,000 peak-normalized underwater spectra (31 horizon-aligned scenes of 1,000 pixels each) and mean spectrum of the sky in zenith above the water. Shading is in SD.

(H) Zebrafish opsin complement (B, blue, G, green; R, red; U, UV), which each opsin template multiplied with the mean underwater spectrum from (G) to estimate relative photon catch rates in nature. Templates are based on [3]; for discussion on spectral positions, see STAR Methods.

(legend continued on next page)

and (2) a custom-built hyperspectral scanner [3, 20] to take 60° full-spectrum images at a lower spatial resolution, matched to that of the larval zebrafish (Figures 1F–1L). We surveyed  $n = 31$  scenes from six field sites in West Bengal, India (Figures S1A and S1B; Data S1).

The action camera data demonstrated that, in these shallow (<50 cm) waters, both the substrate and the water surface are simultaneously viewed by the larvae's wide-angle eyes (Figure 1A) and that the spectrum of light varies strongly with elevation. Directly ahead and to the sides, zebrafish eyes align with a mid-wavelength- ("green") dominated underwater horizon, which divides a long-wavelength- ("red") biased lower visual field and a short-wavelength- ("blue") biased upper visual field of the ground reflecting the underside of the water surface (Figures 1A and S1B–S1D). Beyond ~42° elevation, this reflection gives way to Snell's window [21]—a short-wavelength-biased representation of the 180° world above the water surface compressed into a constant ~97° of visual angle directly above the animal. To estimate which part of the scene contained most chromatic information, we used principal-component analysis (PCA), using red, green, and blue (RGB) pixel values from different elevations. As in terrestrial scenes [5], PC1 reliably captured the achromatic component where the R, G, and B channels co-vary (Figure 1B). Across the entire image, this component always explained >90% of the total variance.

Next, PC2 and PC3 captured the main chromatic axes (red versus blue; green versus blue) in decreasing order of importance (Figures 1C and 1D). Further analysis revealed that the horizon and lower visual field accounted for most chromatic structure, whereas Snell's window above the animal was effectively achromatic (Figure 1E). For this, we horizontally divided each of  $n = 31$  images into 5° stripes and calculated the fraction of the total image variance explained by PC2 and PC3 as a function of elevation (Figure 1E). As our camera was designed for human trichromacy and can therefore only approximate the spectral content available to the zebrafish's tetrachromatic retina [22, 23], we next computed the chromatic image statistics in hyperspectral images taken at the same sites as seen by the larval zebrafish.

### Spectral Positioning of Zebrafish Cone-Opsins under Natural Light

To sample full-spectrum underwater images in the zebrafish natural world, we custom built a hyperspectral scanner [3] comprising a spectrometer and two mirrors mounted on Arduino-controlled servo-motors (Figure 1F) [20]. The system collected 60° full-spectrum (200–1,000 nm) images centered on the underwater horizon. Individual readings were regularly spaced at ~1.6° to approximate the behavioral resolution limit of larval zebrafish [24]. A total of 31 scans of 1,000 "pixels"

each were taken at the same scenes previously photographed with our action camera (Data S1). To estimate what spectral content is available in nature for zebrafish vision, we multiplied the mean of all 31,000 spectra with the animal's cone absorption spectra. Zebrafish larvae express mainly four opsins in their four cone types: long wavelength sensitive (LWS) (548 nm); middle wavelength sensitive (MWS) (467 nm); short wavelength sensitive (SWS) (411 nm); and UV sensitive (UVS) (365 nm; for discussion, see STAR Methods) [22]. For simplicity, we will refer to these as the R, G, B, and "UV" (U) channels, respectively. As expected [25], short wavelengths from the sky illumination were attenuated in the water, resulting in a red shift of the available light (Figure 1G). The peak of the mean underwater spectrum aligned with the absorbance peak of the zebrafish R-opsin (Figure 1H), suggesting that R-cones are strongly driven in the zebrafish's natural habitat and are thus well suited to encode features that require high signal-to-noise representation, such as movement. In contrast, U-cones lay at the extreme short-wavelength end of available light under water. In this regime, the signal power is ~7% compared to the red channel. Investing neural resources despite the low signal power suggests that zebrafish gain important benefits from using this channel. For example, it could aid detecting UV-rich prey [26, 27] against the water's underside internal reflection [21], boost achromatic contrasts against the underwater horizon [28], and more generally support detection of chromatic contrast. Finally, B- (16%) and G-cones (45%) received intermediate numbers of photons and are likely used for both achromatic and chromatic computations alongside the other cones.

### Short- versus Long-Wavelength Computations Carry Most Chromatic Information

We next asked which chromatic contrasts in RGBU opsin space predominate in the natural environment of the zebrafish larvae. For this, we multiplied the spectrum of each pixel with the spectral sensitivity function of each opsin to yield four monochromatic opsin activation images from each scan (Figures 1I, 1J, and S1F; cf. Figure 1A), one for each opsin channel. As predicted from the available light, the R-opsin image showed the most spatial structure, followed by G and B. In contrast, the U-opsin image had a "foggy" appearance, probably due to UV light scattering on dissolved organic matter. Such UV background light can be exploited by animals to detect the UV-dark silhouettes of otherwise difficult to spot objects [28, 29].

Next, to separate achromatic and chromatic content across these four opsin images, we computed PCA across now 4-dimensional RGBU opsin space (like above). This again reliably extracted achromatic luminance information into PC1 and then three chromatic dimensions (PC2–4; Figures 1K and S1E). The mean opsin contrasts obtained by PCA across all  $n = 31$

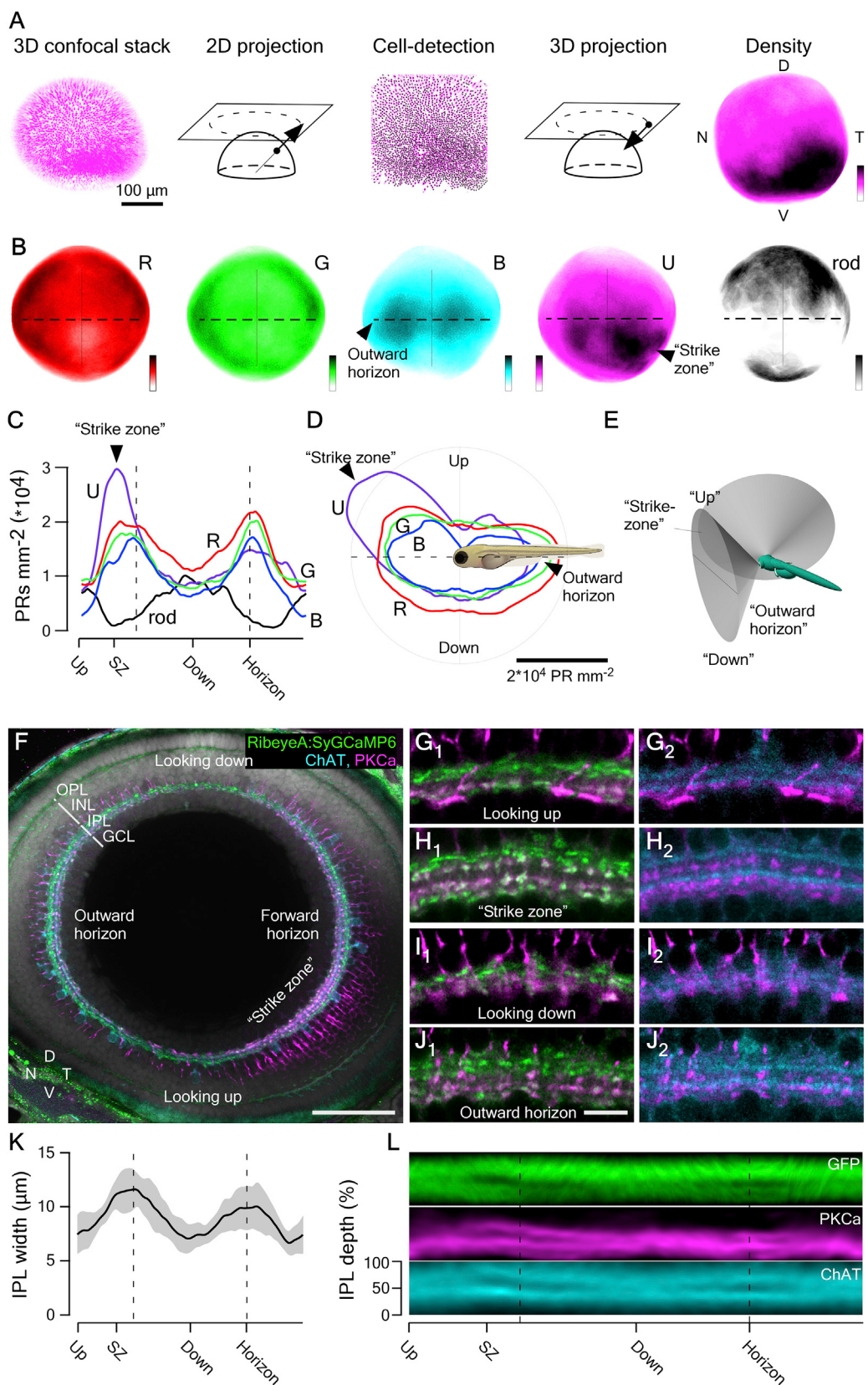
(I and J) Enlargement (I) and reconstruction (J) of photographed scene (A) from scanner data by multiplying each pixel's spectrum with each opsin template (H). Scan reconstructions are truncated beyond 20° from the center to remove sampling edge artifacts.

(K) Mean loadings of PCs 1–4 across all  $n = 31$  scans.

(L) As (E), cumulative variance explained by PCs 2–4 calculated separately for 5° vertical slices across all  $n = 31$  scanned scenes. Error shadings are in SD. As before (E), most chromatic information exists at and below the horizon.

(M and N) Schematic summary of natural chromatic statistics (M) and of expected behaviorally important short-wavelength-specific visual requirements (N). Larval schematic is modified from L. Griffiths.

See also Figure S1 and Data S1.



(legend on next page)

scans were (1) RG/BU (“long- versus short-wavelength opponency”), (2) RU/GB, and (3) RB/GU (complex opponencies). We again cut the images into 5° horizontal stripes and found that the sum of variance explained by the three chromatic dimensions peaked at and below the underwater horizon (Figure 1L; cf. Figure 1E).

The efficient coding hypothesis [8, 30, 31] predicts that the obtained opsin contrasts should also be encoded by retinal neurons, as is the case for human trichromacy [5, 7]. Moreover, these circuits should be biased to retinal regions that survey the horizon and lower visual field, where these chromatic contrasts predominate (Figure 1M). In addition, species-specific visual demands that cannot emerge from the statistics of static scenes, such as the need for prey capture and to avoid predators, may drive the evolution of additional, dedicated circuits. For example, zebrafish larvae feed on “translucent” unicellular paramecia that scatter light in a UV-biased manner [26, 27]. For capture, larvae approach their prey from slightly below and converge the eyes to bring their image into binocular space in front of and just above the horizon [15, 32] but outside Snell’s window (J. Semmelhack, personal communication). In this part of visual space, the paramecium is illuminated by its own Snell’s window and thus—from point of view of the larval zebrafish—broadcasts its position as a UV-bright spot against the underside of the water (Figure 1N) [21]. For surveying this part of visual space (here dubbed “strike zone,” [SZ]), the larval retina should invest in UV-driven prey capture circuits. Finally, detecting UV-dark silhouettes against a UV-bright background should work across the entire upper visual field, including Snell’s window.

Our natural image data and known behavioral demands of larval zebrafish lead to three predictions for how these animals’ retinal circuits should be organized for efficient coding:

- (1) Above the animal, light is short wavelength biased and there is little color information, but the visual input can be used to spot silhouettes—accordingly, circuits should be achromatic or short wavelength biased.
- (2) In the strike zone, the behavioral requirement for prey capture should drive an increased predominance of UV-on circuits.

- (3) Along the horizon, and below the animal, the retina should invest in chromatic circuits, with an emphasis on short- versus long-wavelength computations.

We next set out to test these predictions experimentally. We first assessed the distributions of retinal neurons across the eye and subsequently used *in vivo* functional imaging to study the chromatic organization of the inner retina.

### Anisotropic Photoreceptor Distributions Match the Distribution of Natural Light

To study the distribution of the zebrafish larva’s four cone and one rod photoreceptor types across the retinal surface, we fluorescently labeled individual photoreceptor populations. For R-, B-, and U-cones, we expressed fluorescent proteins under cone-type-specific promoters *thrbc*, *sws2*, and *sws1*, respectively. No line exclusively labeling G-cones was available. Instead, we calculated their distribution by subtracting genetically defined R-cones from retinas where both R- and G-cones were labeled using immunohistochemistry (*zpr-1* antibody) [33]. Finally, rod photoreceptors (rods) were surveyed by expressing mCherry under rod-specific promoter *xops* [34]. We projected each 3D retina as imaged under a confocal microscope into a local-distance-preserving 2D plane, counted photoreceptors, and projected their positions back onto the original semi-sphere to generate density maps of each photoreceptor type across the 3D eye (Figure 2A; STAR Methods).

Unlike in adults, who feature a crystalline photoreceptor mosaic [35], in larvae, all photoreceptor distributions were anisotropic (Figures 2B–2D). The sum of all cones, which made up ~92% of all photoreceptors, peaked at the horizon (Figures 2C and 2D), in line with this part of visual space comprising most chromatic information in nature (Figures 1E and 1I). This bias was mainly driven by R-, G-, and B-cones. In contrast, U-cones peaked ~30° above the forward-facing horizon to form a UV-specialized area centralis [36], possibly to support visual prey capture (Figure 1N). Next, the lower visual field was dominated by R-cones yet closely followed by approximately matched densities all other cones. Like the horizon, this part of visual space could therefore be used for color vision (Figure 1M) but with an additional long-wavelength bias, as observed in nature

### Figure 2. Anisotropic Retinal Structure

- (A) 3D confocal stack taken across the entire retina of an 8 dpf larva (*Tg(Open1sw1:GFP)*) with all U-cones fluorescently labeled was used for semi-automated quantification of cone densities across the retina (STAR Methods).
- (B) Average densities of all four cone types and rods across the retina, based on  $n = 6$  (R), 6 (G), 5 (B), 5 (U), and 4 (rods) retinas (*Tg(thrb:Tomato*) for R; *zpr-1* antibody staining for G; *Tg(-3.5opn1sw2:mCherry)* for B; *Tg(open1sw1:GFP)* for U; and *Tg(xops:ntr-mCherry)* for rod). Color scales: 0 (white)–35,000 (black) cones  $\text{mm}^{-2}$  or 0–9,000 rods  $\text{mm}^{-2}$ . D, dorsal; N, nasal; T, temporal; V, ventral.
- (C–E) To compare cone distributions across retinal positions (C and D), we computed densities at sagittal plane approximately aligned with the back surface of the lens (E; STAR Methods). This plane projects in a ~130° cone from the eye center, with eyes rotated ~36.5° forward during prey capture (18.5° at rest; Figures S2A and S2B). Cone and rod densities across the plane are defined in (E) on a linear scale of the fish’s egocentric visual field. Dashed lines indicate the forward and outward horizon. (D) is as (C), plotted in polar coordinates relative to the body of the fish as indicated.
- (F) Whole-eye immunostaining of an 8 dpf *Tg(-1.8ctbp2:SyGCaMP6)* larvae labeled against GFP (bipolar cell [BC] terminals, green), choline acetyltransferase (ChAT) (cholinergic amacrine cells, cyan), and protein kinase C alpha (PKC $\alpha$ ) (on-BCs, magenta). Shown is the same sagittal section used in (F)–(H). PKC $\alpha$ -stained BC somata are only faintly visible as the chosen equalization was tuned to highlight the much more strongly labeled synaptic terminals in the strike zone. The scale bar represents 50  $\mu\text{m}$ . GCL, ganglion cell layer; INL, inner nuclear layer; IPL, inner plexiform layer; OPL, outer plexiform layer.
- (G–J) Higher magnification sections from (F) showing the IPL at different positions across the eye as indicated. For clarity, GFP/PKC $\alpha$  (G<sub>1</sub>–J<sub>1</sub>) and ChAT/PKC $\alpha$  (G<sub>2</sub>–J<sub>2</sub>) are shown separately. Looking up (G), “strike zone” (H), looking down (I), and outward horizon (J). The scale bar represents 5  $\mu\text{m}$ .
- (K) Mean IPL thickness across  $n = 5$  whole-eye immunostainings as in (F).
- (L) Mean signal in the three fluorescence channels as above.

See also Figure S2.

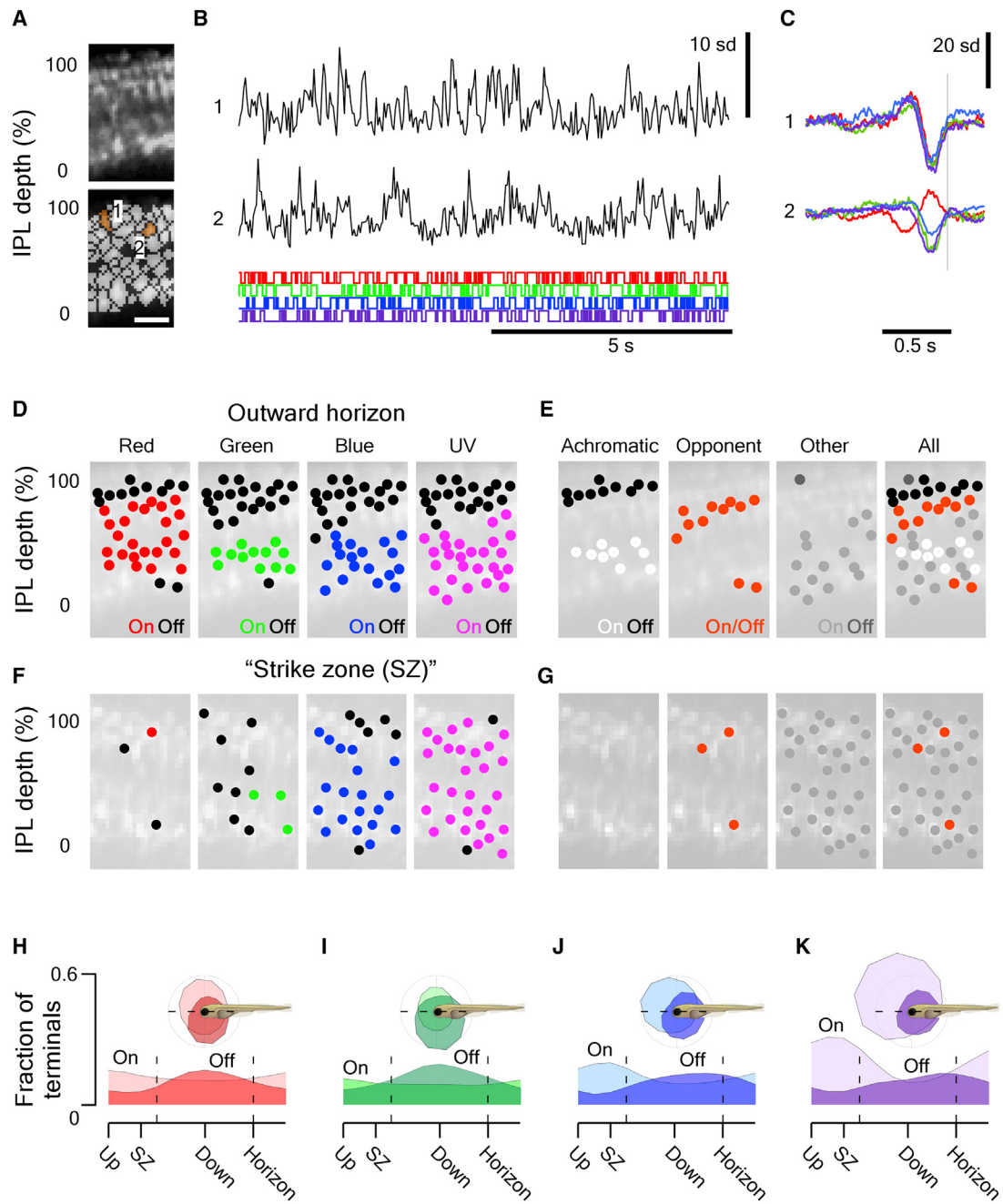


**Figure 3. Surveying Inner Retinal Chromatic Responses In Vivo**

(A) 2-photon scan field ( $32 \times 64$  pixels; 15.625 Hz) of a nasal IPL section (outward horizon) in a *Tg(-1.8ctbp2:SyGCaMP6)* larvae for simultaneous recording of light-driven calcium responses across the entire IPL depth at single-terminal resolution (top) and regions of interest (ROIs) (bottom). The scale bar represents 5  $\mu\text{m}$ .

(B) Example of calcium responses to tetrachromatric binary white noise stimulation (12.8 Hz; STAR Methods) of two ROIs highlighted in (A).

(C) Tetrachromatric linear filters (“kernels”) recovered by reverse correlation of each ROI’s response with the noise stimulus (B). The color code indicates the stimulus channel (R, G, B, U; cf. Figure S3A).

(D) For each stimulus channel, we classified each ROI’s kernel as either “on” (in red, green, blue, or purple), “off” (black), or non-responding (no marker) and plotted each response over the anatomical scan image (STAR Methods).

(E) By comparison across the four stimulus channels, we then classified each ROI as either achromatic off (R+G+B+U off, black) or on (R+G+B+U on, white), Color opponent (any opposite polarity responses in a single ROI, orange) or “other” (gray) and again plotted each ROI across the IPL to reveal clear chromatic and achromatic layering in this scan is shown.

(legend continued on next page)

(Figure S1D). In contrast, the upper visual field comprised fewest cones of any type but instead had an increased number of rods. Unlike cones, rods near exclusively looked straight up through the effectively achromatic but bright Snell's window or straight down, which may support the detection of optic flow on the ground, even in dim light, and/or allow telling the distance to the ground for maximal camouflage for predation from above. Accordingly, already at the level of photoreceptor distributions, the retina of larval zebrafish exhibits a series of anisotropies that align well with the major spectral trends in their visual world and their behavioral demands. How are these anisotropies reflected in the inner retina?

### An Anisotropic Inner Retina

To survey inner retinal structure, we immunolabeled the intact eyes of 7 or 8 dpf *Tg(–1.8ctbp2:SyGCaMP6)* larvae against GFP (green, all bipolar cell [BC] terminals [37], choline acetyl-transferase [ChAT]; blue, starburst amacrine cells [SACs] [38] and phosphokinase C alpha [PKC $\alpha$ ]; magenta, on BCs [38]) and imaged them across the sagittal plane aligned with the back surface of the lens in the 3D eye (STAR Methods). In larval zebrafish, the full monocular field of view is  $\sim 163^\circ$ , and at rest, eyes are rotated forward by  $\sim 18.5^\circ$  ( $\sim 35.5^\circ$  during prey capture) [15, 32]. The surveyed sagittal plane samples the visual world in a cone of  $\sim 130^\circ$  (Figures 2E and S2) such that its temporal extreme projects in front of the fish whereas the nasal extreme projects outward and backward along the horizon. Dorsal and ventral positions survey the visual world at  $\sim 65^\circ$  elevation below and above the animal, respectively. For simplicity, all visual field coordinates are given in egocentric space from the point of view of the fish: up (ventral); SZ (temporo-ventral); down (dorsal); and outward horizon (nasal).

Our data on inner retinal structure consolidated and extended all large-scale anisotropies set up by the photoreceptors (Figures 2F–2L). Like cone densities (Figures 2C and 2D), also inner retinal thickness varied nearly 2-fold with position, with the thickest inner plexiform layer (IPL) segments aligning with the horizons (Figures 2F and 2K). Alongside, the number, distribution, shapes, and sizes of synaptic terminals varied with eye position. For example, whereas PKC $\alpha$  labeling highlighted three strata in the strike zone (one between and two below the ChAT bands; Figure 2H2), circuits surveying the world above the animal appeared to have only the two lower strata (Figure 2I2). Here, the lowest band featured particularly large BC terminals that are characteristic for teleost “mixed” BCs that process inputs from rod photoreceptors [39]—in agreement with the anisotropic distribution of rods (Figure 2C). In addition, there were PKC $\alpha$ -negative terminals at the IPL bottom that were restricted to the strike zone (Figures 2H and 2L). SAC processes also varied with position. For example, the neat bilayer of ChAT immunoreactivity in the strike zone and for looking outward (Figures 2H2 and 2J2) disappeared into a “haze” in circuits looking down (Figures 2I2 and 2L). Additional, albeit more subtle, differences included var-

iations in PKC $\alpha$  expression and the sharpness of overall lamination between the forward and outward horizons (Figures 2F and 2L). Clearly, the larval zebrafish retina features a broad range of anatomical specializations across the visual field. How are these anatomical specializations reflected in function? To address this question, we next turned to calcium imaging of BC terminals across the eye.

### The Inner Retina Is Divided into Anisotropic Chromatic and Achromatic Layers

We used 2-photon *in vivo* imaging of light-driven activity in retinal BCs expressing the genetically encoded calcium sensor GCaMP6f under the *ctbp2* (*ribeyeA*) promoter fused to the synaptic protein synaptophysin [40]. We focused on BCs [41] as (1) they directly and differentially collect inputs from all photoreceptors to form the basis of color vision [39, 42], (2) they are the only neuron class that contacts all other neurons in the retina, and (3) they directly drive retinal ganglion cells, the eye's connection to the brain. Individual pre-synaptic terminals of BCs can be resolved while imaging the entire depth of the inner retina [40] (Figure 3A).

To estimate each BC terminal's chromatic sensitivity, we used a tetrachromatic “noise” stimulus (Figures 3B and 3C). Specifically, each of four light-emitting diodes (LEDs) that were spectrally matched to the absorption peaks of the four cone opsins (Figure S3A) were presented to the live larvae through the objective and flickered in a known random binary sequence at 12.8 Hz (Figure 3B). Using reverse correlation [43], we then recovered four temporal response kernels for each BC terminal [44], one for each LED, and thus effective cone-type input (Figure 3C). This revealed different chromatic sensitivities in different BC terminals. For example, some terminals displayed near-equal sensitivity to all four LEDs, indicating a wavelength-invariant response preference (achromatic terminals; Figures 3A–3C, region of interest [ROI] 1). Other terminals had kernels with opposite polarity across LEDs (color opponent terminals; Figures 3A–3C, ROI 2). In an example scan from the “outward horizon” for all opsin channels, the majority of off and on responses occurred in the upper and lower part of the IPL, respectively (Figures 3D and 3E), in line with mammalian inner retinal circuits [41, 44–46]. However, the transition depth between on and off bands differed between cone channels, with the R-channel transitioning closer to the inner nuclear layer (INL) than the other three. As a result, two achromatic bands at the top (RGBU<sub>Off</sub>, black) and in the center (RGBU<sub>On</sub>, white) of the IPL were separated by a layer of R<sub>On</sub>/G<sub>On</sub>/B<sub>On</sub> color-opponent responses (orange; Figure 3E). Additional R(G)<sub>Off</sub>/B<sub>On</sub> opponent responses occurred at the lower edge of the IPL. The remaining response types were classified as “other” and were mostly confined to the on channel in the lower part of the IPL (gray). Accordingly, in this part of the eye, the inner retina was organized into distinct functional layers. Moreover, as predicted from natural light, all color-opponent terminals computed short- versus long-wavelength chromatic

(F and G) As (D) and (E), respectively, but for a scan taken in the temporo-ventral retina, which surveys the world in front of the animal just above the visual horizon. This zone is critical for prey capture and was thus dubbed “strike zone”.

(H–K) Distribution of all on and off responses per stimulus channel (H, red; I, green; J, blue; and K, UV) based on n = 4,099/6,565 ROIs that passed a minimum quality criterion (STAR Methods) sampled from across the entire sagittal plane (115 scans, 12 fish).

See also Figure S3.

contrasts. However, this functional layering was not consistently observed in other parts of the retina. In an example scan taken from the strike zone, nearly all terminals exhibited strong U(B)-on responses that reached far into the upper sublamina, whereas responses to R and G stimulation all but disappeared (**Figures 3F** and **3G**)—in striking agreement with the predicted need for dedicated UV-on prey-capture circuits in this part of the eye.

Together, these two examples demonstrate that the larval zebrafish IPL is functionally highly anisotropic. To systematically assess how BC responses are distributed across the eye and which specific chromatic and color-opponent computations predominate, we recorded from a total of  $n = 6,568$  synaptic terminals across the sagittal plane ( $n = 115$  scans, 12 fish at 7 or 8 dpf), out of which  $n = 4,099$  (62%) that passed a quality criterion (**Figures S3B** and **S3C**; **STAR Methods**) were used for further analysis. All recordings were taken in the same sagittal plane used for anatomy (cf. **Figure 2F**). This dataset showed that the zebrafish larval retina is functionally highly anisotropic (**Figures 3H–3K**; cf. **Figure S3D**). For example, independent of wavelength, on and off responses were systematically biased to the upper and lower visual fields, respectively. Here, a disproportionate number of  $U_{\text{On}}$  responses surveyed the strike zone (**Figure 3K**). What is the functional distribution of BCs across the larval zebrafish eye and what do they encode?

### Large-Scale Functional Anisotropies of the Inner Retina Match Natural Spectral Statistics

To assign BCs to functional clusters, we used a Mixture of Gaussian model to sort terminals independent of eye position based on their full temporo-chromatic response kernels (**Figure 4**; **STAR Methods**). BC terminals fell into  $n = 26$  clusters, which were further grouped into four major response groups:  $n = 5$  achromatic clusters ( $C_{1–5}$ ; **Figure 4A**);  $n = 9$  UV(B)-monochromatic clusters ( $C_{6–14}$ ; **Figure 4B**);  $n = 6$  chromatic clusters ( $C_{15–20}$ ; **Figure 4C**);  $n = 5$  color opponent clusters ( $C_{21–25}$ ; **Figure 4D**); and  $n = 1$  discard cluster ( $C_x$ ; **Figure 4E**; **STAR Methods**). These groups were defined based on the relative amplitudes and polarities of each cluster mean's four chromatic kernels (**STAR Methods**): equal polarity equal gain (achromatic); equal polarity different gain (chromatic and UV(B)-monochromatic); or different polarity (color opponent). In addition, we distinguished UV(B)-monochromatic clusters from other chromatic clusters in view of the hypothesized behavioral relevance of such a channel (**Figure 1N**). Their abundance and extreme short-wavelength bias indicate the existence of a dedicated UV system that is not integrated with other chromatic retinal circuits.

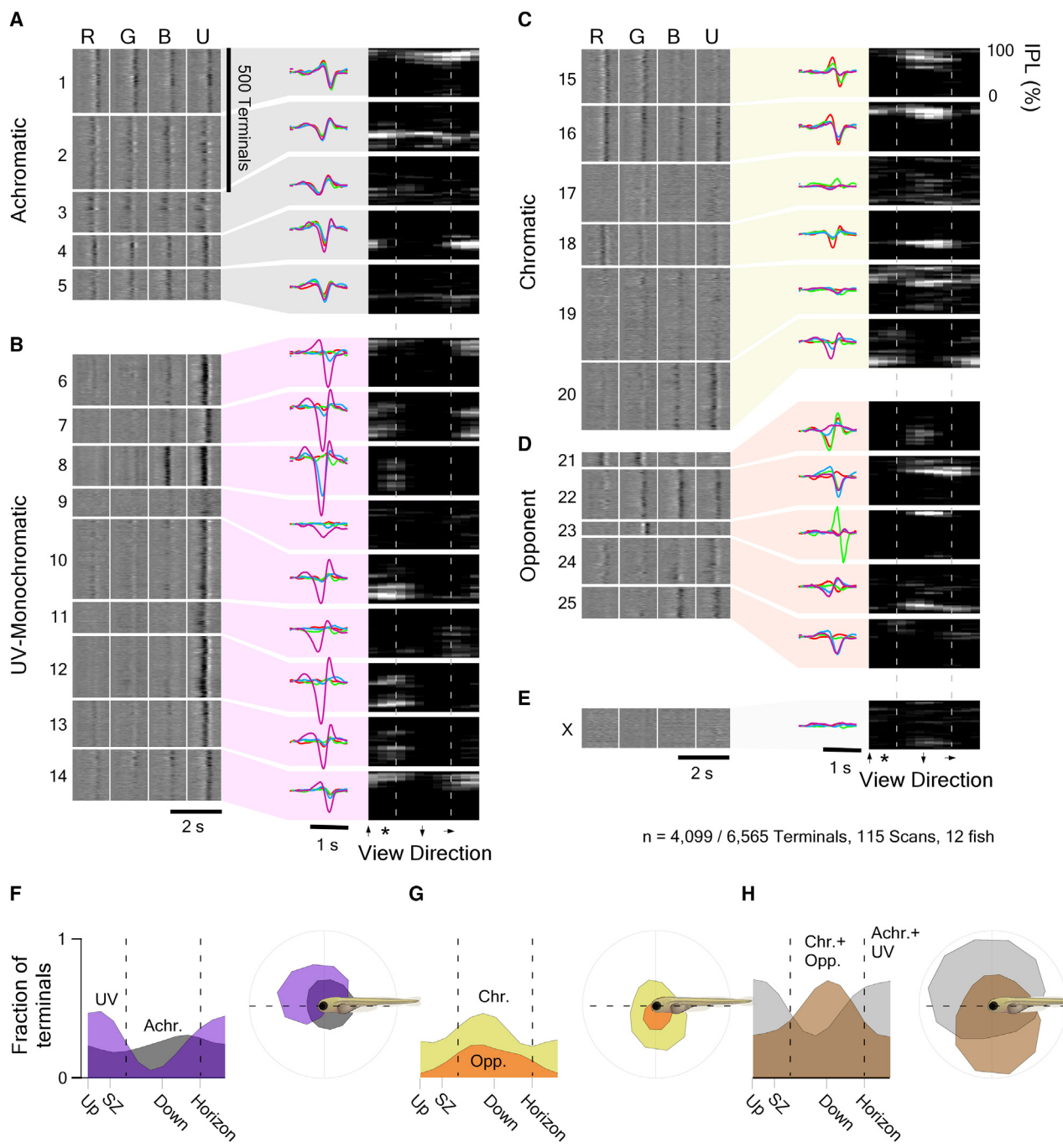
For each cluster, we computed the anatomical distribution across the eye and IPL depth (right insets). This revealed that no functional BC cluster, nor any major functional group (**Figures 4F–4H**), was uniformly distributed across the entire field of view. Instead, most clusters predominated in either the upper or lower visual field, with some clusters in addition exhibiting a secondary bias to predominately looking forward or outward. In agreement with our predictions, all UV(B)-monochromatic clusters were strongly biased to the upper and forward-facing visual field (**Figures 4B** and **4F**), whereas all color-opponent clusters were skewed toward the lower and outward-facing visual field (**Figures 4D** and **4G**). In fact, there were effectively no color-opponent terminals that survey the world directly upward through

the nearly achromatic Snell's window. Together, all circuits potentially dealing with color (all chromatic and opponent clusters) surveyed the lower and outward horizontal visual field, whereas all circuits likely to deal with achromatic computations (all UV(B)-monochromatic and achromatic clusters) were skewed toward the upper and frontal visual field (**Figure 4H**). Moreover, four out of five color-opponent clusters computed short- versus long-wavelength chromatic antagonisms (reminiscent of PC2 from natural scenes), whereas the remaining single cluster ( $C_{23}$ ) compared G to all other channels (reminiscent of a mix of PCs 3 and 4; **Figure 4D**; cf. **Figure 1K**). This set of functional anisotropies of the larval zebrafish inner retinal circuitry is in strong agreement with the distribution of behaviorally meaningful chromatic content in nature (**Figures 1M** and **1N**).

### The Functional Layering of the Larval Zebrafish Inner Retina

Next, we assessed how different response types were distributed across the layers of the IPL (**Figure 5**). Unlike in mammals [41], BCs in most non-mammalian vertebrates, including zebrafish, can have mono-, bi-, and tri-stratified morphologies [39, 47]. In agreement, terminals falling into individual clusters were mostly distributed across 1–3 major IPL bands (**Figures 4A–4E**, right insets), indicating that each could principally be linked to a single or small number of BC types. To establish the major trends in functional organization of the IPL, we subdivided each of the four major response groups (achromatic, UV-monochromatic, chromatic, and color opponent) into their “on” and “off”-dominated response types and assessed the distribution of each of the resultant eight groups across the depth of the IPL for different positions in the eye (**Figure 5A**).

Most response groups (**Figure 5A**; rows 2–9) were largely restricted to subsets of the larval zebrafish's six anatomical IPL layers (row 1, black). However, some functions were distributed more broadly than others. For example, most achromatic on terminals (row 3, gray) occurred just beneath the outer ChAT band (ganglion cell layer [GCL] side) and could be found in any eye position—albeit at varying densities. In contrast, UV(B)-monochromatic on terminals occurred across the entire outer part of the IPL (layers 3–6) but remained near exclusively restricted to the upper visual field (row 5, lilac). Other “functions” were tightly restricted in both visual field and IPL depth. For example, color-opponent off-dominated terminals were near exclusively found in layers 1 and 3 and only in the lower visual field (row 8, brown). Next, we again combined on and off versions of each response group for clarity and superimposed the resulting four histograms of the four response groups for different eye positions (**Figures 5B** and **5C**). Looking up, each IPL layer contained a substantial fraction of UV(B)-monochromatic terminals; only in layers 2 and 5, there were more chromatic and achromatic terminals, respectively (**Figure 5B1**). In the strike zone, this UV(B) dominance further intensified and shifted toward the off bands in the lower IPL—in line with UV-on circuits aiding the detection of paramecia (**Figure 5B2**; cf. **Figure 1N**). In contrast, there were effectively no UV-monochromatic terminals looking down, and the IPL appeared more neatly divided into layers differentially encoding color-opponent, chromatic, and achromatic information (**Figure 5B3**). Finally, IPL circuits surveying the outward horizon had approximately balanced numbers of terminals from each

**Figure 4. The Functional Organization of the Larval Zebrafish Eye**

Mixture of Gaussian clustering of all n = 4,099 responding terminals based on the full waveforms of their tetrachromatic kernels, with cluster number limited by the Bayesian Information Criterion (BIC), yielded 25 clusters (C<sub>1-25</sub>) and 1 discard cluster (C<sub>x</sub>).

(A–D) For simplicity, each cluster was further allocated to one of four major response groups (STAR Methods): (A) achromatic (C<sub>1-5</sub>); (B) UV(B)-monochromatic (C<sub>6-14</sub>); (C) chromatic (C<sub>15-20</sub>); and (D) color opponent (C<sub>21-25</sub>).

(E) Discard cluster C<sub>x</sub>. For each cluster, shown are the time courses of each kernel (left heatmaps; lighter shades indicating higher values), the cluster means (middle), and their anatomical distribution across IPL depth (y axis) and position in the eye (x axis; right heatmaps; lighter shades indicate higher abundance). Dashed lines indicate the forward and outward horizon; the asterisk denotes the position of the strike zone. The height of each cluster's left heatmap indicates its number of allocated terminals.

(F–H) Linear (left) and polar (right) histograms of terminal abundance of the functional groups defined in (A)–(E) across the larval zebrafish's visual space. (F) UV(B)-monochromatic (purple) and achromatic (gray) groups, (G) chromatic (yellow) and color-opponent (orange) groups, and (H) summed UV(B)-monochromatic and achromatic groups (gray) versus chromatic and color opponent groups (brown) are shown.

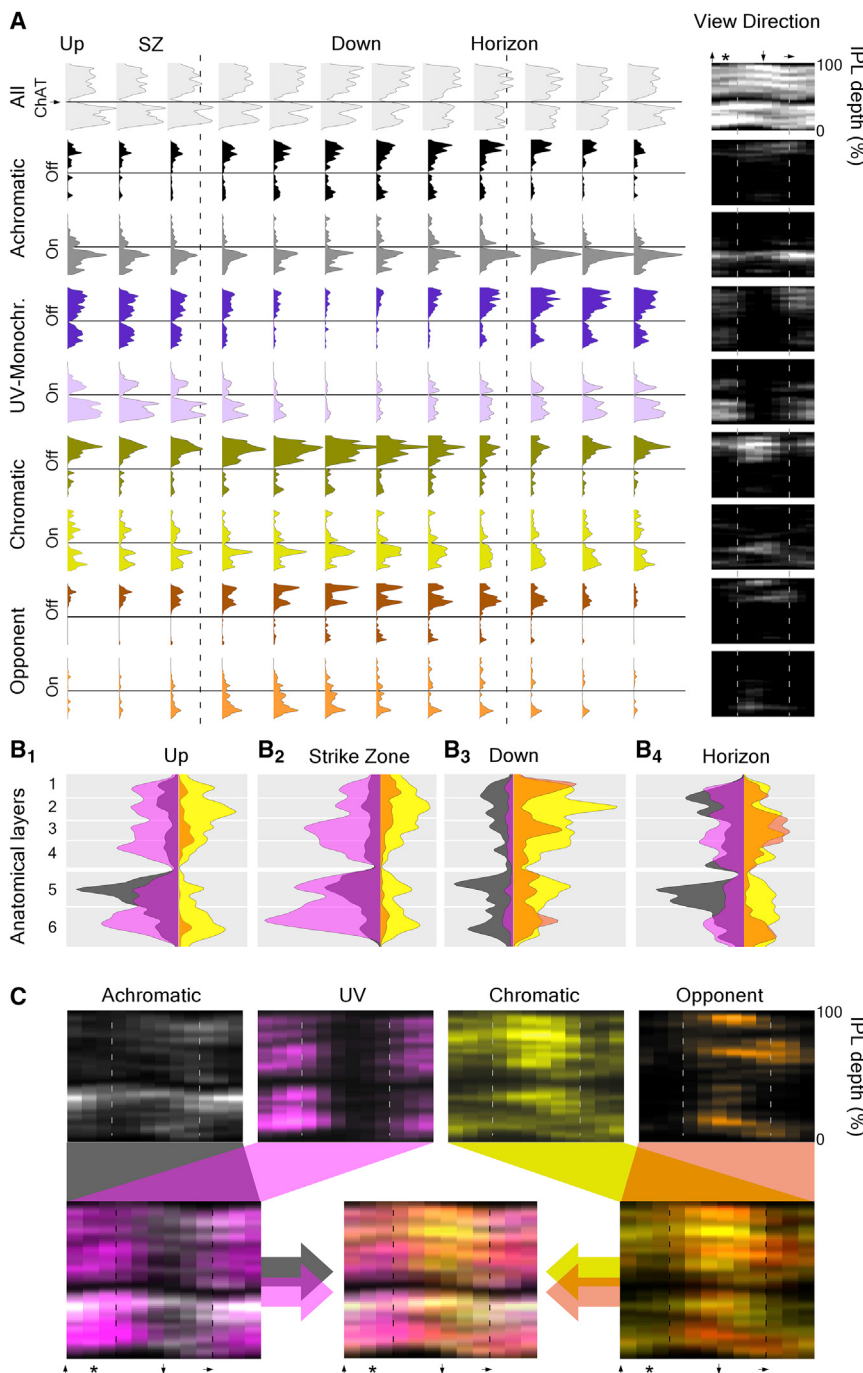


**Figure 5. Distribution of Function across the IPL**

(A) Histograms of terminal abundance across IPL depth (y axis) and position in the eye (set of histograms) for each functional group (cf. Figure 7), divided by on- and off-dominated responses as indicated. In addition, the distribution of all  $n = 6,565$  scanned terminals independent of response quality is plotted to reveal the anatomical distribution of all BC terminals (top, light gray). Heatmaps to the right show the same data in a single image. Asterisk denotes the position of the strike zone. Dashed lines indicate the forward and outward visual horizon. Solid horizontal lines indicate the position of the lower ChAT band as an anatomical reference.

(B<sub>1-4</sub>) On and off-collapsed histograms of the four response groups for four example regions (down, dorsal; outward horizon, nasal as indicated; strike zone, temporo-ventral; up, ventral) summarize the functional IPL layering across eye positions, with approximate anatomical layers indicated in the background shading. For clarity, achromatic and UV(B)-monochromatic histograms are x axis reversed.

(C) Color-coded response groups (top) plotted against eye position (x) and IPL depth (y) and merge (bottom). Throughout, colors indicate the functional groups: achromatic (gray and black); UV(B)-monochromatic (purple and violet); chromatic (yellow and beige); and color opponent (orange and brown).

“IPL streaks” around the lower and outward visual field (Figure 5C, bottom right). In contrast, only ~5 such IPL streaks with UV or achromatic function could be discerned around the strike zone (Figure 5C, bottom left). This suggests that the lower and outward-looking part of the eye harbors more diverse BC circuits than what is required in much more “simple”-appearing circuits surveying the upper and frontal visual field.

A neat division of function into specific layers of the IPL for surveying the ground and outward horizon, though novel in its chromatic scope and complexity, is consistent with current knowledge on the functional organization of the vertebrate inner retina [41, 44–46]. However,

functional group and a similarly neat functional organization with IPL depth as observed for the lower visual field (Figure 5B4).

The complexity of functional layers differed markedly, in particular between the strike zone and upper visual field (Figures 5B1, 5B2, and 5C), compared to the lower visual field and outward horizon (Figures 5B3, 5B4, and 5C). In the latter, the total number of peaks often used as a tell-tale for individual IPL strata far exceeded the 6 traditionally used anatomical layers of the larval zebrafish IPL. For example, chromatic and opponent layers alone appeared to set up ~10 interdigitated functional

overrepresentation of the UV(B) channel in the upper and frontal visual fields, despite the presence of all other cone types, is striking. Here, most visual functions appear to draw near exclusively on on and off UV(B)-monochromatic channels at the expense of both color vision and the off achromatic channel. How does the eye build this rich functional division across visual space?

#### Building a Functionally Anisotropic Retina

Across all vertebrate retinas studied to date, there are distinct types of BCs, each with a unique anatomy, synaptic connections,

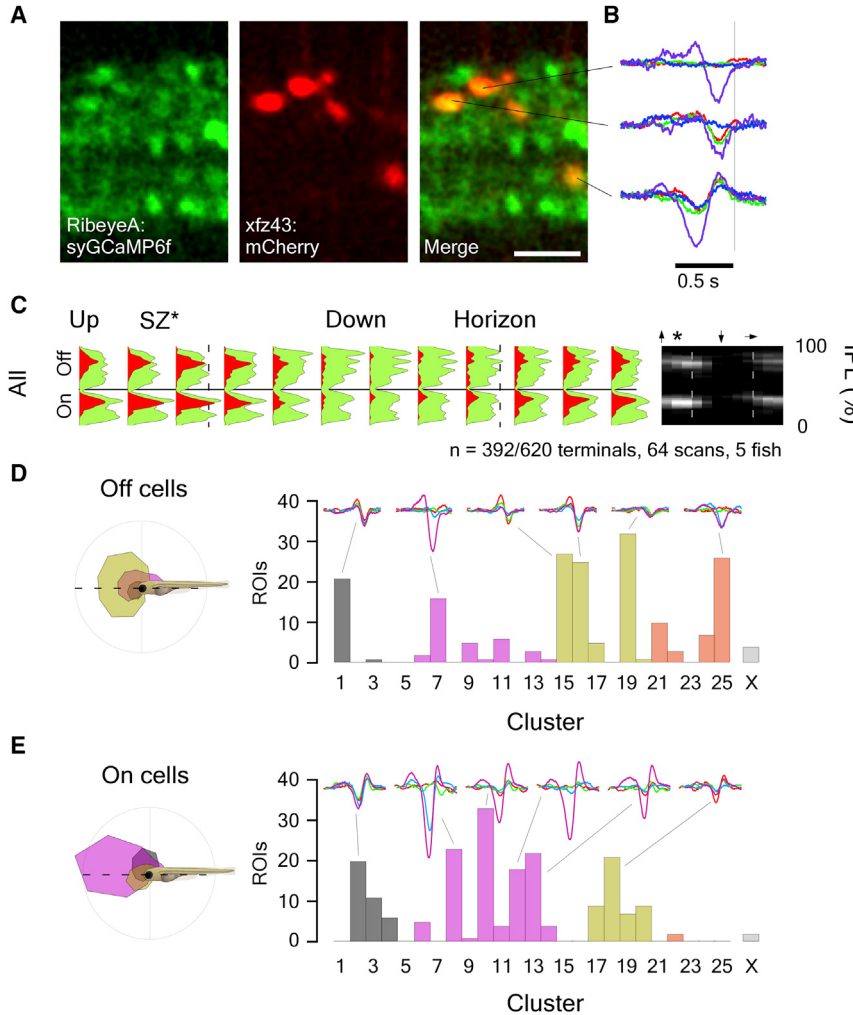


**Figure 6. Distribution of xfz43-Expressing BC Types**

(A) High-resolution 2-photon scan of a ventro-nasal (up and outward) IPL section in 7 dpf larvae expressing SyGCaMP6f under *ctbp2* promoter (green) as well as mCherry under *xfz43* (red). The scale bar represents 5  $\mu$ m.

(B) Subsequent higher rate scans during light stimulation allowed recovering tetrachromatic kernels from individual *xfz43*-positive terminals as before (right).

(C) Distribution of 392/620 *xfz43*-positive BC terminals (64 scans, 5 fish) that passed our response criterion (red; STAR Methods) across the IPL (y) and eye (x), superimposed on the distribution of all terminals from the same scans (green). The heatmap on the right shows only *xfz43*-positive terminals. Dashed lines indicate the forward and outward horizon, whereas the solid horizontal line indicates the position of the lower ChAT band.

(D) Allocation of all *xfz43*-positive anatomical off terminals to functional clusters (right) and distribution of these terminals across the eye by functional group (left).

(E) As (D) but for *xfz43*-positive anatomical on cells. See also Figure S4.

and functional properties (reviewed in [41]). Both larval and adult zebrafish have ~20 morphologically distinct BC types, with a broad diversity of chromatic connections to cones in the outer retina [39, 47], many more than the dichromatic mouse [42, 48–50]. Two non-mutually exclusive design strategies may underlie the observed set of functional anisotropies; first, different types of BCs with different functions might specifically exist only in certain parts of the retina [51, 52]. This hypothesis is, for example, supported by the absence of the characteristic large terminals of on-type mixed BCs outside the ventral- and dorsal-most retina (Figures 2H and 2J), where rods are located (Figures 2B and 2C). Second, the same types of BCs may exist across the entire retina but shifting function with position [3, 53–55].

We set out to explore these two possibilities experimentally. For this, we used the *xfz43* marker line, which labels at least three morphologically well-characterized presumed types of BCs with different, known anatomical connections in the outer retina [56]. Here, our definition of “neuron type” includes that these neurons all express *xfz43* and, in addition, form three consistent morphologies at the level of both dendrites and axonal ramifications. Of these three, one off- and one on-stratifying *xfz43*-positive BC type each preferentially contacts R- and G-cones across their

large dendritic fields. Both are thus predicted to exhibit a RG-biased physiology. A third, smaller on-stratifying *xfz43* type indiscriminately samples from all cones and is therefore expected to encode on-achromatic features.

To selectively record from these cells’ synaptic terminals, we crossed our *Tg(−1.8ctbp2:SyGCaMP6)* line to *Tg(xfz43:Gal4;UAS:ntr-mCherry)* animals (Figures 6A and 6B). As before, this al-

lowed recording from all BC terminals, but in addition, labeled *xfz43*-cells are simultaneously recorded in the red fluorescence channel. This dataset (64 scans, 5 fish) represents a subset of the complete BC survey presented previously (Figures 3, 4, and 5) and consisted of n = 620 *xfz43*-positive terminals, of which the 392 (63%) that passed our quality criterion (STAR Methods) fell into 2 main IPL bands (Figure 6C, red).

Next, we functionally assessed *xfz43* off- and on-stratifying terminals separately. In agreement with their stratification, off- and on-stratifying terminals fell into functional off and on clusters, respectively (Figures 6D, 6E, and S4). However, the presumed single *xfz43* off type [56] fell into 6+ functional clusters that spanned all four major functional groups (Figure 6D). Similarly, the presumed two on-type *xfz43* cells were sorted into 6+ clusters that spanned 3 major functional groups (Figure 6E). In fact, individual examples clearly demonstrated this functional diversity within a morphological type, irrespective of any clustering (not shown). This extreme functional diversity of all three presumed “clean,” morphologically defined BC types suggests that, in the larval zebrafish eye, a neuron’s functional identity can be strongly shaped by its surrounding neuronal network in different parts of the eye.

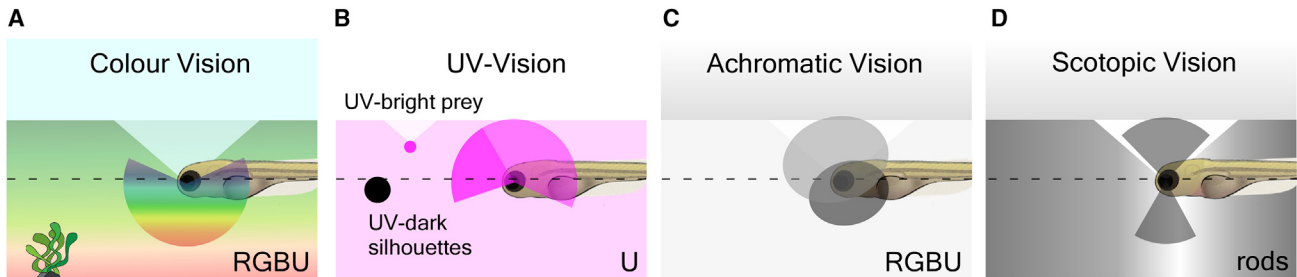


**Figure 7. The Larval Zebrafish Eye's Chromatic Organization for Vision in Nature**

(A) Circuits for color vision are generally biased to the horizon and lower visual field, where most chromatic content is found in nature.  
 (B) Circuits for UV(B)-monochromatic vision dominate the upper and frontal visual field and may be used for prey capture and the detection of UV-dark silhouettes against a UV-bright background.  
 (C) Achromatic circuits are found throughout the eye, with on and off circuits dominating the upper-frontal- and lower-outward-facing visual fields, respectively.  
 (D) Rod circuits are exclusively used to survey the sky directly above and the ground reflection directly beneath the animal, where most photons can be caught. In each image, the triangular area above the animal depicts Snell's window, and the visual horizon is indicated by a dashed line.

However, the allocation of *xfz43* cells to functional clusters was far from random. For example, *xfz43* off-terminal allocated clusters C<sub>1</sub>, C<sub>15</sub>, and C<sub>17</sub> all exhibited at least a small RG bias, consistent with these cells' known connectivity in the outer retina [56]. Similarly, cluster C<sub>18</sub>, which captured most chromatic *xfz43* on terminals, had an RG-biased physiology, whereas the largely achromatic cluster C<sub>2</sub> might reflect the cone-unselective *xfz43* cells. In each case, this mainly leaves several UV(B)-dominated response clusters that are not explained by these cells' cone selectivity (C<sub>6–8,12,13</sub>).

Are these UV clusters generated by UV cone inputs with unusually high gain? For example, the small on-type *xfz43* cell indiscriminately integrates the outputs of fewer than 10 cones [56]. Here, a hypothetical high-gain UV input from only two or three cones could bias a cell toward a UV-dominated response. Whereas this hypothesis clearly needs further exploration, already here several lines of evidence point at this as one mechanism of functional diversification across the larval zebrafish IPL. First, under natural light, U-cones receive ~15 times fewer photons than red cones (Figure 1H), prompting the need for a high-gain amplification system for short-wavelength visual processing. In agreement, in mice, the gain of U-cones appears to be higher than that of M-cones [3, 57]. Second, U-cones numerically dominate the frontal and upper visual field (Figures 2B–2D). Third, UV responses overall dominate the IPL in this part of the eye (Figures 3K, 4B, 4F, and 5), with their kernel amplitudes often exceeding those of any other opsin channels more than 10-fold, despite the presence of all other cone types. Taken together, it therefore seems likely that, at least to some extent, larval zebrafish BC types with specific function exist in only parts of the eye but that, in addition, more large-scale outer- and/or inner-retinal circuits can "override" this basic functional organization.

## DISCUSSION

We have shown that inner-retinal circuits of larval zebrafish are exquisitely matched to their natural visual environment on several levels. First, chromatic circuits are systematically integrated by a neatly layered inner retina but only at the horizon and the lower visual fields, which in nature contain the most chro-

matic information (Figure 7A; cf. Figures 1E, 1K, 4G, 4H, and 5B). Here, the chromatic computations performed by these circuits match the differential predominance of different natural chromatic contrasts and behavioral demands (Figures 4D and 1K). The upper and frontal visual fields are dominated by UV-driven circuits, a specialization that begins with an anisotropic arrangement of U-cones across the eye (Figures 2B–2D) and is mirrored across the temporo-ventral inner retina, apparently at the expense of circuits serving color vision and neat inner retinal organization (Figure 7B; cf. Figures 3K, 4F, and 5). This UV dominance is likely linked to the need to spot nearby UV-bright microorganisms [26] as well as the ability to detect UV-dark objects on the backdrop of further UV-bright organic matter dissolved in the water [28, 58, 59]. Achromatic cone-driven circuits are used across the entire visual field but differentially use on- and off-dominant regions in the upper and lower visual field, respectively, possibly to drive the dorsal righting response, which helps fish maintain an upright posture by aligning their vertical body axis with the brightness gradient of light from the sky (Figure 7C; cf. Figures 3H–3K). Finally, rod-driven circuits exclusively survey the visual field above and below the animal, likely to capitalize on the additional light caught through Snell's window and its ground reflections (Figure 7D; cf. Figure 2B, right). Importantly, these specializations reliably occur in lab animals that have never been exposed to the zebrafish natural habitat, suggesting that they are deeply hardwired into the developmental programs. Our results also highlight a need to critically evaluate existing literature on larval zebrafish retinal anatomy, development, and function in view of possible variations with retinal position. To what extent the set of striking regional specialization of the larval zebrafish visual system is already established in the outer retina and how it is used in the retinal output and brain to ultimately drive behavior will be important to address in future studies.

Finally, as zebrafish grow up, they explore deeper and more rapidly moving waters with distinct spectral statistics and different predators compared to the slow-moving shallow waters inhabited by larvae. Alongside, zebrafish switch to a more varied diet that includes insects floating on the water surface [19] that appear as dark silhouettes against a bright background. For efficient coding, adult retinal function should reflect these changing visual demands. Whereas systematic cross-retina physiological

studies of adults are currently lacking, some insights may be gained from anatomy. Unlike larvae, adults feature a crystalline receptor mosaic with fixed 2:2:1:1 R:G:B:U stoichiometry [35], which may provide a more balanced chromatic input structure across the retina. However, the “adult strike zone’s” elevated retinal ganglion cell density [60] hints at a continued use of this part of the retina for specialized visual tasks. In the future, it will be important to explore the extent and nature of possible retinal specializations in zebrafish adults.

## STAR★METHODS

Detailed methods are provided in the online version of this paper and include the following:

- KEY RESOURCE TABLE
- CONTACT FOR REAGENT AND RESOURCE SHARING
- EXPERIMENTAL MODEL AND SUBJECT DETAILS
  - Animals and tissue preparation
  - Choice of age of zebrafish larvae
  - The cone-opsin complement of zebrafish
- METHOD DETAILS
  - Field sites
  - Hyperspectral imaging
  - Two-photon Ca<sup>2+</sup> imaging and light stimulation
  - Immunohistochemistry
  - Photoreceptor densities
  - The number of neurons in the 7–8 dpf larval zebrafish
- QUANTIFICATION AND STATISTICAL ANALYSES
  - Data analysis
  - Pre-processing and receptive field mapping
  - Feature extraction and Clustering
  - Grouping of clusters into response groups
  - Histograms against eye position
- DATA AND SOFTWARE AVAILABILITY

## SUPPLEMENTAL INFORMATION

Supplemental Information includes four figures and one data file and can be found with this article online at <https://doi.org/10.1016/j.cub.2018.04.075>.

## ACKNOWLEDGMENTS

We thank Kripan Sarkar and Fredrik Jutfeld for help with field work, Leon Lagano for the provision of zebrafish lines and critical feedback, and Thomas Euler for critical feedback. The authors would also like to acknowledge support from the FENS-Kavli Network of Excellence. Funding was provided by the European Research Council (ERC-StG “NeuroVisEco” 677687 to T.B.), Marie Curie Skłodowska Actions individual fellowship (“ColourFish” 748716 to T.Y.), Marie Skłodowska-Curie European Training network “Switchboard” (Switchboard receives funding from the European Union’s Horizon 2020 research and innovation programme under the Marie Skłodowska-Curie grant agreement no. 674901), The Deutsche Forschungsgemeinschaft (DFG) (BA 5283/1-1 to T.B. and BE 5601/4-1 to P.B.), The Medical Research Council (MC\_PC\_15071 to T.B.), and the Federal Ministry of Education and Research of Germany through the Bernstein Award for Computational Neuroscience (FKZ 01GQ1601 to P.B.).

## AUTHOR CONTRIBUTIONS

M.J.Y.Z., N.E.N., T.Y., and T.B. designed the study, with help from D.-E.N., D.O., and P.B.; M.J.Y.Z. and T.Y. performed 2-photon imaging experiments

and immunohistochemistry; T.Y. generated all novel zebrafish lines; N.E.N. and T.B. built the hyperspectral scanner and performed field work; N.E.N., M.J.Y.Z., and T.Y. performed pre-processing with inputs from T.B.; P.B. developed the clustering framework; T.B. analyzed the data with help from all authors; and T.B. wrote the manuscript with help from P.B. and input from all authors.

## DECLARATION OF INTERESTS

The authors declare no competing interests.

Received: January 18, 2018

Revised: April 18, 2018

Accepted: April 24, 2018

Published: June 21, 2018

## REFERENCES

1. Land, M., and Nilsson, D.-E. (2012). *Animal Eyes* (Oxford University Press).
2. Cronin, T.W., Johnsen, S., Marshall, N.J., and Warrant, E.J. (2014). *Visual Ecology*, First Edition (Princeton University Press).
3. Baden, T., Schubert, T., Chang, L., Wei, T., Zaichuk, M., Wissinger, B., and Euler, T. (2013). A tale of two retinal domains: near-optimal sampling of achromatic contrasts in natural scenes through asymmetric photoreceptor distribution. *Neuron* 80, 1206–1217.
4. Yilmaz, M., and Meister, M. (2013). Rapid innate defensive responses of mice to looming visual stimuli. *Curr. Biol.* 23, 2011–2015.
5. Lewis, A., and Zhaoping, L. (2006). Are cone sensitivities determined by natural color statistics? *J. Vis.* 6, 285–302.
6. Ruderman, D.L., Cronin, T.W., and Chiao, C.-C. (1998). Statistics of cone responses to natural images: implications for visual coding. *J. Opt. Soc. Am. A Opt. Image Sci. Vis.* 15, 2036–2045.
7. Buchsbaum, G., and Gottschalk, A. (1983). Trichromacy, opponent colours coding and optimum colour information transmission in the retina. *Proc. R. Soc. Lond. B Biol. Sci.* 220, 89–113.
8. Simoncelli, E.P., and Olshausen, B.A. (2001). Natural image statistics and neural representation. *Annu. Rev. Neurosci.* 24, 1193–1216.
9. Wong, K.Y., and Dowling, J.E. (2005). Retinal bipolar cell input mechanisms in giant danio. III. ON-OFF bipolar cells and their color-opponent mechanisms. *J. Neurophysiol.* 94, 265–272.
10. Easter, S.S., Jr., and Nicola, G.N. (1996). The development of vision in the zebrafish (*Danio rerio*). *Dev. Biol.* 180, 646–663.
11. Preuss, S.J., Trivedi, C.A., vom Berg-Maurer, C.M., Ryu, S., and Bollmann, J.H. (2014). Classification of object size in retinotectal microcircuits. *Curr. Biol.* 24, 2376–2385.
12. Trivedi, C.A., and Bollmann, J.H. (2013). Visually driven chaining of elementary swim patterns into a goal-directed motor sequence: a virtual reality study of zebrafish prey capture. *Front. Neural Circuits* 7, 86.
13. Semmelhack, J.L., Donovan, J.C., Thiele, T.R., Kuehn, E., Laurell, E., and Baier, H. (2014). A dedicated visual pathway for prey detection in larval zebrafish. *eLife* 3, e04878.
14. Dunn, T.W., Gebhardt, C., Naumann, E.A., Riegler, C., Ahrens, M.B., Engert, F., and Del Bene, F. (2016). Neural circuits underlying visually evoked escapes in larval zebrafish. *Neuron* 89, 613–628.
15. Bianco, I.H., Kampff, A.R., and Engert, F. (2011). Prey capture behavior evoked by simple visual stimuli in larval zebrafish. *Front. Syst. Neurosci.* 5, 101.
16. Avdesh, A., Chen, M., Martin-Iverson, M.T., Verdile, G., Mondal, A., and Martins, R.N. (2010). Natural Colour Preference in the Zebrafish (*Danio rerio*). In *Proceedings of Measuring Behavior 2010* (Eindhoven, the Netherlands, August 24–27, 2010), A.J. Spink, F. Grieco, O.E. Krips, L.W.S. Loijens, L.P.J.J. Noldus, and P.H. Zimmerman, eds. (Wageningen: Noldus Information Technology), pp. 155–157.

17. Arunachalam, M., Raja, M., Vijayakumar, C., Malaiammal, P., and Mayden, R.L. (2013). Natural history of zebrafish (*Danio rerio*) in India. *Zebrafish* 10, 1–14.
18. Spence, R., Gerlach, G., Lawrence, C., and Smith, C. (2008). The behaviour and ecology of the zebrafish, *Danio rerio*. *Biol. Rev. Camb. Philos. Soc.* 83, 13–34.
19. Engeszer, R.E., Patterson, L.B., Rao, A.A., and Parichy, D.M. (2007). Zebrafish in the wild: a review of natural history and new notes from the field. *Zebrafish* 4, 21–40.
20. Nevala, N.E., and Baden, T. (2017). A low-cost hyperspectral scanner for natural imaging above and under water. *bioRxiv*. <https://doi.org/10.1101/322172>.
21. Janssen, J. (1981). Searching for zooplankton just outside Snell's window. *Limnol. Oceanogr.* 26, 1168–1171.
22. Chinen, A., Hamaoka, T., Yamada, Y., and Kawamura, S. (2003). Gene duplication and spectral diversification of cone visual pigments of zebrafish. *Genetics* 163, 663–675.
23. Endeman, D., Klaassen, L.J., and Kamermans, M. (2013). Action spectra of zebrafish cone photoreceptors. *PLoS ONE* 8, e68540.
24. Haug, M.F., Biehlmaier, O., Mueller, K.P., and Neuhauss, S.C. (2010). Visual acuity in larval zebrafish: behavior and histology. *Front. Zool.* 7, 8.
25. Chiao, C.C., Cronin, T.W., and Osorio, D. (2000). Color signals in natural scenes: characteristics of reflectance spectra and effects of natural illuminants. *J. Opt. Soc. Am. A Opt. Image Sci. Vis.* 17, 218–224.
26. Novales Flamarique, I. (2012). Opsin switch reveals function of the ultraviolet cone in fish foraging. *Proc. Biol. Sci.* 280, 20122490.
27. Novales Flamarique, I. (2016). Diminished foraging performance of a mutant zebrafish with reduced population of ultraviolet cones. *Proc. Biol. Sci.* 283, 20160058.
28. Losey, G.S., Cronin, T.W., Goldsmith, T.H., Hyde, D., Marshall, N.J., and McFarland, W.N. (1999). The UV visual world of fishes: a review. *J. Fish Biol.* 54, 921–943.
29. Cronin, T.W., and Bok, M.J. (2016). Photoreception and vision in the ultraviolet. *J. Exp. Biol.* 219, 2790–2801.
30. Attneave, F. (1954). Some informational aspects of visual perception. *Psychol. Rev.* 61, 183–193.
31. Barlow, H.B. (1961). Possible principles underlying the transformation of sensory messages. In *Sensory Communication* (MIT), pp. 217–234.
32. Patterson, B.W., Abraham, A.O., MacIver, M.A., and McLean, D.L. (2013). Visually guided gradation of prey capture movements in larval zebrafish. *J. Exp. Biol.* 216, 3071–3083.
33. Larison, K.D., and Bremiller, R. (1990). Early onset of phenotype and cell patterning in the embryonic zebrafish retina. *Development* 109, 567–576.
34. Fadool, J.M. (2003). Development of a rod photoreceptor mosaic revealed in transgenic zebrafish. *Dev. Biol.* 258, 277–290.
35. Engström, K. (1960). Cone types and cone arrangements in the retina of some cyprinids. *Acta Zool.* 41, 277–295.
36. Schmitt, E.A., and Dowling, J.E. (1999). Early retinal development in the zebrafish, *Danio rerio*: light and electron microscopic analyses. *J. Comp. Neurol.* 404, 515–536.
37. Johnston, J., Ding, H., Seibel, S.H., Esposti, F., and Lagnado, L. (2014). Rapid mapping of visual receptive fields by filtered back projection: application to multi-neuronal electrophysiology and imaging. *J. Physiol.* 592, 4839–4854.
38. Nevin, L.M., Taylor, M.R., and Baier, H. (2008). Hardwiring of fine synaptic layers in the zebrafish visual pathway. *Neural Dev.* 3, 36.
39. Li, Y.N., Tsujimura, T., Kawamura, S., and Dowling, J.E. (2012). Bipolar cell-photoreceptor connectivity in the zebrafish (*Danio rerio*) retina. *J. Comp. Neurol.* 520, 3786–3802.
40. Dreosti, E., Odermatt, B., Dorostkar, M.M., and Lagnado, L. (2009). A genetically encoded reporter of synaptic activity in vivo. *Nat. Methods* 6, 883–889.
41. Euler, T., Haverkamp, S., Schubert, T., and Baden, T. (2014). Retinal bipolar cells: elementary building blocks of vision. *Nat. Rev. Neurosci.* 15, 507–519.
42. Behrens, C., Schubert, T., Haverkamp, S., Euler, T., and Berens, P. (2016). Connectivity map of bipolar cells and photoreceptors in the mouse retina. *eLife* 5, 1206–1217.
43. Chichilnisky, E.J. (2001). A simple white noise analysis of neuronal light responses. *Network* 12, 199–213.
44. Franke, K., Berens, P., Schubert, T., Bethge, M., Euler, T., and Baden, T. (2017). Inhibition decorrelates visual feature representations in the inner retina. *Nature* 542, 439–444.
45. Masland, R.H. (2001). The fundamental plan of the retina. *Nat. Neurosci.* 4, 877–886.
46. Wässle, H. (2004). Parallel processing in the mammalian retina. *Nat. Rev. Neurosci.* 5, 747–757.
47. Connaughton, V.P., and Nelson, R. (2000). Axonal stratification patterns and glutamate-gated conductance mechanisms in zebrafish retinal bipolar cells. *J. Physiol.* 524, 135–146.
48. Helmstaedter, M., Briggman, K.L., Turaga, S.C., Jain, V., Seung, H.S., and Denk, W. (2013). Connectomic reconstruction of the inner plexiform layer in the mouse retina. *Nature* 500, 168–174.
49. Greene, M.J., Kim, J.S., and Seung, H.S.; EyeWires (2016). Analogous convergence of sustained and transient inputs in parallel on and off pathways for retinal motion computation. *Cell Rep.* 14, 1892–1900.
50. Wässle, H., Puller, C., Müller, F., and Haverkamp, S. (2009). Cone contacts, mosaics, and territories of bipolar cells in the mouse retina. *J. Neurosci.* 29, 106–117.
51. Zhang, Y., Kim, I.-J., Sanes, J.R., and Meister, M. (2012). The most numerous ganglion cell type of the mouse retina is a selective feature detector. *Proc. Natl. Acad. Sci. USA* 109, E2391–E2398.
52. Bleckert, A., Schwartz, G.W., Turner, M.H., Rieke, F., and Wong, R.O.L. (2014). Visual space is represented by nonmatching topographies of distinct mouse retinal ganglion cell types. *Curr. Biol.* 24, 310–315.
53. Joesch, M., and Meister, M. (2016). A neuronal circuit for colour vision based on rod-cone opponency. *Nature* 532, 236–239.
54. Chang, L., Breuninger, T., and Euler, T. (2013). Chromatic coding from cone-type unselective circuits in the mouse retina. *Neuron* 77, 559–571.
55. Sabbah, S., Gemmer, J.A., Bhatia-Lin, A., Manoff, G., Castro, G., Siegel, J.K., Jeffery, N., and Berson, D.M. (2017). A retinal code for motion along the gravitational and body axes. *Nature* 546, 492–497.
56. D'Orazi, F.D., Zhao, X.F., Wong, R.O., and Yoshimatsu, T. (2016). Mismatch of synaptic patterns between neurons produced in regeneration and during development of the vertebrate retina. *Curr. Biol.* 26, 2268–2279.
57. Breuninger, T., Puller, C., Haverkamp, S., and Euler, T. (2011). Chromatic bipolar cell pathways in the mouse retina. *J. Neurosci.* 31, 6504–6517.
58. Nava, S.S., An, S., and Hamil, T. (2011). Visual detection of UV cues by adult zebrafish (*Danio rerio*). *J. Vis.* 11, 2.
59. Goldsmith, T.H. (1994). Ultraviolet receptors and color vision: evolutionary implications and a dissonance of paradigms. *Vision Res.* 34, 1479–1487.
60. Pita, D., Moore, B.A., Tyrrell, L.P., and Fernández-Juricic, E. (2015). Vision in two cyprinid fish: implications for collective behavior. *PeerJ* 3, e1113.
61. Zhao, X.-F., Ellingsen, S., and Fjose, A. (2009). Labelling and targeted ablation of specific bipolar cell types in the zebrafish retina. *BMC Neurosci.* 10, 107.
62. Takechi, M., Hamaoka, T., and Kawamura, S. (2003). Fluorescence visualization of ultraviolet-sensitive cone photoreceptor development in living zebrafish. *FEBS Lett.* 553, 90–94.
63. Salbreux, G., Barthel, L.K., Raymond, P.A., and Lubensky, D.K. (2012). Coupling mechanical deformations and planar cell polarity to create regular patterns in the zebrafish retina. *PLoS Comput. Biol.* 8, e1002618.
64. Suzuki, S.C., Bleckert, A., Williams, P.R., Takechi, M., Kawamura, S., and Wong, R.O.L. (2013). Cone photoreceptor types in zebrafish are generated

- by symmetric terminal divisions of dedicated precursors. *Proc. Natl. Acad. Sci. USA* **110**, 15109–15114.
65. Karlsson, J., von Hofsten, J., and Olsson, P.E. (2001). Generating transparent zebrafish: a refined method to improve detection of gene expression during embryonic development. *Mar. Biotechnol. (NY)* **3**, 522–527.
  66. McLean, D.L., and Fetscho, J.R. (2011). Movement, technology and discovery in the zebrafish. *Curr. Opin. Neurobiol.* **21**, 110–115.
  67. Hoon, M., Okawa, H., Della Santina, L., and Wong, R.O.L. (2014). Functional architecture of the retina: development and disease. *Prog. Retin. Eye Res.* **42**, 44–84.
  68. Orger, M.B. (2016). The cellular organization of zebrafish visuomotor circuits. *Curr. Biol.* **26**, R377–R385.
  69. Friedrich, R.W., Jacobson, G.A., and Zhu, P. (2010). Circuit neuroscience in zebrafish. *Curr. Biol.* **20**, R371–R381.
  70. Keller, P.J., Ahrens, M.B., and Freeman, J. (2015). Light-sheet imaging for systems neuroscience. *Nat. Methods* **12**, 27–29.
  71. Hildebrand, D.G.C., Cicconet, M., Torres, R.M., Choi, W., Quan, T.M., Moon, J., Wetzel, A.W., Scott Champion, A., Graham, B.J., Randlett, O., et al. (2017). Whole-brain serial-section electron microscopy in larval zebrafish. *Nature* **545**, 345–349.
  72. Allison, W.T., Hairberger, T.J., Hawryshyn, C.W., and Temple, S.E. (2004). Visual pigment composition in zebrafish: evidence for a rhodopsin-porphyrinopsin interchange system. *Vis. Neurosci.* **21**, 945–952.
  73. Hunt, D.M., Wilkie, S.E., Bowmaker, J.K., and Poopalasundaram, S. (2001). Vision in the ultraviolet. *Cell. Mol. Life Sci.* **58**, 1583–1598.
  74. Takechi, M., and Kawamura, S. (2005). Temporal and spatial changes in the expression pattern of multiple red and green subtype opsin genes during zebrafish development. *J. Exp. Biol.* **208**, 1337–1345.
  75. Enright, J.M., Toomey, M.B., Sato, S.Y., Temple, S.E., Allen, J.R., Fujiwara, R., Kramlinger, V.M., Nagy, L.D., Johnson, K.M., Xiao, Y., et al. (2015). Cyp27c1 red-shifts the spectral sensitivity of photoreceptors by converting Vitamin A1 into A2. *Curr. Biol.* **25**, 3048–3057.
  76. Koskelainen, A., Ala-Laurila, P., Fyhrquist, N., and Donner, K. (2000). Measurement of thermal contribution to photoreceptor sensitivity. *Nature* **403**, 220–223.
  77. Loew, E.R., and Dartnall, H.J.A. (1976). Vitamin A1/A2-based visual pigment mixtures in cones of the rudd. *Vision Res.* **16**, 891–896.
  78. Douglas, R.H., and McGuigan, C.M. (1989). The spectral transmission of freshwater teleost ocular media—an interspecific comparison and a guide to potential ultraviolet sensitivity. *Vision Res.* **29**, 871–879.
  79. Siebeck, U.E., and Marshall, N.J. (2001). Ocular media transmission of coral reef fish—can coral reef fish see ultraviolet light? *Vision Res.* **41**, 133–149.
  80. Euler, T., Hausselt, S.E., Margolis, D.J., Breuninger, T., Castell, X., Detwiler, P.B., and Denk, W. (2009). Eyecup scope—optical recordings of light stimulus-evoked fluorescence signals in the retina. *Pflugers Arch.* **457**, 1393–1414.
  81. Dorostkar, M.M., Dreosti, E., Odermatt, B., and Lagnado, L. (2010). Computational processing of optical measurements of neuronal and synaptic activity in networks. *J. Neurosci. Methods* **188**, 141–150.
  82. Li, Y.N., Matsui, J.I., and Dowling, J.E. (2009). Specificity of the horizontal cell-photoreceptor connections in the zebrafish (*Danio rerio*) retina. *J. Comp. Neurol.* **516**, 442–453.
  83. Vitorino, M., Jusuf, P.R., Maurus, D., Kimura, Y., Higashijima, S., and Harris, W.A. (2009). Vsx2 in the zebrafish retina: restricted lineages through derepression. *Neural Dev.* **4**, 14.
  84. Song, P.I., Matsui, J.I., and Dowling, J.E. (2008). Morphological types and connectivity of horizontal cells found in the adult zebrafish (*Danio rerio*) retina. *J. Comp. Neurol.* **506**, 328–338.
  85. Robles, E., Laurell, E., and Baier, H. (2014). The retinal projectome reveals brain-area-specific visual representations generated by ganglion cell diversity. *Curr. Biol.* **24**, 2085–2096.
  86. Naumann, E.A., Kampff, A.R., Prober, D.A., Schier, A.F., and Engert, F. (2010). Monitoring neural activity with bioluminescence during natural behavior. *Nat. Neurosci.* **13**, 513–520.
  87. Baden, T., Berens, P., Franke, K., Román Rosón, M., Bethge, M., and Euler, T. (2016). The functional diversity of retinal ganglion cells in the mouse. *Nature* **529**, 345–350.

**STAR★METHODS****KEY RESOURCE TABLE**

REAGENT or RESOURCE	SOURCE	IDENTIFIER
Antibodies		
Zpr1	ZIRC	N/A
Anti-GFP	AbCam	13970
Anti-ChAT	Chemicon	AB144P
Anti-PKC $\alpha$	Sigma	P4334
Anti-chichken IgG CF488A	Sigma	SAB4600031-50UL
Anti-rabbit IgG CF568	Sigma	SAB4600076-50UL
Anti-goat IgG DyLight650	BETHYL	A50-207D5
Anti-mouse IgG DyLight647	Jackson Immunoresearch Laboratories	715-606-150
Chemicals, Peptides, and Recombinant Proteins		
1-phenyl-2-thiourea (PTU)	Sigma	P7629-10G
Agarose low melting point	Fisher Scientific	BP1360-100
$\alpha$ -bungarotoxin	Tocris	2133
16% Paraformaldehyde	Agar Scientific	AGR1026
VectaShield	Vector	H-1000
Experimental Models: Organisms/Strains		
Zebrafish: Tg(Gal4-VP16,UAS:EGFP) ub43	[61]	N/A
xfz43:Gal4		
Zebrafish: Tg(UAS-E1b::NTR-mCherry) c264	[61]	N/A
UAS:NTR-mCherry		
Zebrafish: Tg(-1.8ctbp2a:Rno.Syp-GCaMP6) uss1 -1.8ctbp2:SyGCaMP6	[62]	N/A
Zebrafish: Tg(-5.5opn1sw1:EGFP) kj9	[62]	N/A
Opn1sw1:GFP		
Zebrafish: Tg(-3.2opn1sw2:mCherry) mi2007	[63]	N/A
Zebrafish: Tg(thrb:Tomato)q22	[64]	N/A
Recombinant DNA		
XopsEGFP-N1	[32]	N/A
Software and Algorithms		
Igor Pro 6.3	WaveMetrics	N/A
Fiji	NIH	N/A
Python 3.5	N/A	N/A

**CONTACT FOR REAGENT AND RESOURCE SHARING**

Further information and requests for resources and reagents should be directed to and will be fulfilled by the Lead Contact, Tom Baden ([t.baden@sussex.ac.uk](mailto:t.baden@sussex.ac.uk)).

**EXPERIMENTAL MODEL AND SUBJECT DETAILS****Animals and tissue preparation**

All procedures were performed in accordance with the UK Animals (Scientific Procedures) act 1986 and approved by the animal welfare committee of the University of Sussex. For all experiments, we used 7-8 days post fertilization (*dpf*) zebrafish (*Danio rerio*) larvae of either sex. The following transgenic lines were used: *Tg(-1.8ctbp2:SyGCaMP6)*, *Tg(xfz43:Gal4;UAS:ntr-mCherry;-1.8ctbp2:SyGCaMP6)* [61], *Tg(opn1sw1:GFP)* [62], *Tg(-3.2opn1sw2:mCherry)* [63], *Tg(thrb:Tomato)* [64]. In addition, a *Tg(xops:ntr-mCherry)* line was generated by injecting pXops-nfsB-mCherry plasmid into one-cell stage eggs and subsequently screening for the expression of mCherry among progenies of injected fish. pXops-nfsB-mCherry plasmid was constructed by replacing EGFP with nfsB-mCherry in XopsEGFP-N1 plasmid [34].

Owing to the exploratory nature of our study, we did not use randomization and blinding. Animals were housed under a standard 14:10 day/night rhythm and fed 3 times a day. Animals were grown in 200  $\mu$ M 1-phenyl-2-thiourea (Sigma) from 1 *dpf* to prevent melanogenesis [65]. For 2-photon *in-vivo* imaging, zebrafish larvae were immobilised in 2% low melting point agarose (Fisher Scientific, Cat: BP1360-100), placed on the side on a glass coverslip and submerged in fish water. Eye movements were further prevented by injection of  $\alpha$ -bungarotoxin (1 nL of 2 mg/ml; Tocris, Cat: 2133) into the ocular muscles behind the eye. For immunohistochemistry, larvae were culled by tricaine overdose (800 mg/l) at 7–8 *dpf*. Whole larvae were fixed in 4% paraformaldehyde for 25 min before being washed in phosphate-buffered saline (PBS).

### Choice of age of zebrafish larvae

Throughout this work we used 7–8 *dpf* zebrafish larvae of either sex. At this age, zebrafish brain and retina conform to the anatomical structures of vertebrate nervous system, such as existence of canonical cell types and specific neural circuits [66, 67]. Supported by their visual circuits, 7–8 *dpf* zebrafish larvae perform a wide range of behaviors including reflexive responses as well as prey-capture and predator avoidance [68, 69], allowing them to feed independently, navigate their environment and avoid predators. Though under constant development, larval zebrafish of this age are therefore fully autonomous and highly visual animals. They have been used extensively to study vertebrate nervous system organization and function including benchmark studies of whole-brain functional imaging [70] and serial-section electron microscopy [71].

### The cone-opsin complement of zebrafish

While larval (and adult) zebrafish have four cone-types and one rod-type, each cone's *in vivo* action spectrum depends on several factors, including which opsin gene(s) are expressed, which retinal chromophore(s) are used, and what fraction of the spectrum of light is filtered out by the optical apparatus. To justify the choice of opsin templates used (cf. [Figure S3A](#)) we will discuss each in turn.

Zebrafish have UV, blue, green and red sensitive cones in their retina. The maximal absorbance ( $\lambda_{\max}$ ) for the UV sensitive cones (UVS) lies around 360–365 nm while the  $\lambda_{\max}$  for the blue sensitive cones (SWS, short wavelength sensitive cone) is at 411 nm [72, 73]. For green and red cones (medium and long wavelength sensitive cones, MWS and LWS) the situation is more complex since these cones can express different types of opsins. Zebrafish use four MWS-cone opsins (RH2-1, RH2-2, RH2-3 and RH2-4) and two LWS-cone opsins (LWS1 and LWS2) [22]. All these opsins have different spectral sensitivities, and all are expressed in the retina [74]. This variation is expected in a small spectral sensitivity shift in these cones with retinal position. Based on the abundance of the opsin type across the retina for the green and red cones during the early development of zebrafish larvae, we chose the most abundant opsin type in each case: the RH2-1 gene ( $\lambda_{\max}$  at 467 nm) for the green cones and the LWS1 gene ( $\lambda_{\max}$  at 548 nm) for the red cones.

In addition, vertebrates can use two different chromophores: 11-cis-retinal (vitamin A1) and 11-cis-3,4-didehydroretinal (vitamin A2). The A2 chromophore holds one extra double bond compared to A1, which lowers the energy needed to initiate the phototransduction cascade [75–77]. By changing the chromophore from A1 to A2, a visual pigment's peak spectral sensitivity can be shifted to longer wavelengths. While for UVS- and SWS-opsins, this switch has little effect, MWS-opsins can be shifted by 20 nm, while LWS-opsins shift up to 60 nm [72]. This change can be triggered in adult zebrafish when treated with thyroid hormone [72, 75], but there is no clear evidence for the zebrafish of any age holding the A2 chromophore under normal conditions. We therefore assumed that only the A1 chromophore is present. As such,  $\lambda_{\max}$  values for the cone templates were set to 365 nm, 411 nm, 467 nm and 548 nm for the four cone types, respectively.

Other possible structures in the eye filtering the light reaching the light sensitive cells are the cornea, the lens and the vitreous body. All these parts can hold patches of pigments that mostly absorb shorter wavelengths (UV) affecting the spectrum of light that eventually reaches the photoreceptors [78]. Whether or not the animal has these pigments varies widely across different species [79], but measurements are still lacking for the larval zebrafish. Notably, here the small size of the eye, and the fact that UV-cones exist throughout the retina, strongly suggest that UV-filtering by the optical apparatus in these animals is negligible. As such, we did not correct our opsin templates for any putative spectral related to the optical apparatus of the eye.

## METHOD DETAILS

### Field sites

Six field sites were visited in West Bengal, India ([Figure S1](#); [Data S1](#)) in May 2017, just before the monsoon season. The global positioning coordinates of each site were: Site 1 (lat. 26.531390, long. 88.669265), site 2 (lat. 26.528117, long. 88.641474), site 3 (lat. 26.841041, long. 88.828882), site 4 (lat. 26.792305, long. 88.588003), site 5 (lat. 26.903202, long. 88.554333) and site 6 (lat. 26.533690, long. 88.648729). Zebrafish of all ages were found mostly in shallow pools of water adjacent to bigger streams (with exception of one deeper fish farm pond, site 6), in agreement with previous work [17, 18]. The visited sites varied substantially with the type of habitat (different sized streams, stagnant fish farm pond), the amount of vegetation above and under water, the type of substrate and the current of the water. For analysis, all recorded data was combined without prior selection.

### Hyperspectral imaging

To gather hyperspectral images, we used a custom made, water-proofed hyperspectral scanner [20] built around a commercial spectrometer (Thorlabs CCS200/M, 200–1,000 nm). In short, two spectrally broad mirrors mounted on top of servo-motors were controlled by an Arduino Uno microcontroller to iteratively bring different positions in visual space into the active part of the

spectrometer to build up a complete hyperspectral image [3]. 1,000 Scan-points were spaced 1.6° and defined by a Fermat's spiral, followed by a custom path-shortening algorithm. Spectra were recorded using the spectrometer software OSA (Thorlabs). We used diving-weights to stabilize the scanner under water. In addition, the scanner-case was placed inside a hard-plastic box to maintain the upright position with a UV-transparent window pointing forward. After placing the scanner to its < 50 cm depth underwater position, we waited up to 5 minutes for any stirred-up debris to settle. All n = 31 scans were taken during the day between 11am and 5pm; the weather conditions varied from slightly cloudy to clear sky but remained constant for individual measurements. Time for one scan acquisition varied between 4 and 8 minutes, depending on the set mirror-move times (200-500 ms) and integration times (80-200 ms) which were adjusted for each measurement to yield an approximately consistent signal-to-noise independent of absolute light intensity in each scene. Finally, in each case in addition to the scan a 180° still image was taken approximately at the scanner position with an action camera (Campark ACT80 3K 360°). Stills were mapped to the 2D plane by a standard angular fisheye projection to 720x720 pixels (0.25° per pixel).

### Two-photon Ca<sup>2+</sup> imaging and light stimulation

We used a MOM-type two-photon microscope (designed by W. Denk, MPI, Martinsried; purchased through Sutter Instruments/Science Products). Design and procedures were described previously [80]. In brief, the system was equipped with a mode-locked Ti:Sapphire laser (Chameleon Vision-S, Coherent) tuned to 927 nm, two fluorescence detection channels for GCaMP6f (F48x573, AHF/Chroma) and mCherry (F39x628, AHF/Chroma), and a water immersion objective (W Plan-Apochromat 20x/1.0 DIC M27, Zeiss). For imaging mCherry, we used 960 nm excitation instead. For image acquisition, we used custom-written software (ScanM, by M. Mueller, MPI, Martinsried and T. Euler, CIN, Tuebingen) running under IGOR pro 6.3 for Windows (Wavemetrics), taking 64 × 32 pixel image sequences (15.625 frames per s) for activity scans or 512 × 512 pixel images for high-resolution morphology scans.

For light stimulation (Figure S3A), we focused a custom-built stimulator through the objective, fitted with band-pass-filtered light-emitting diodes (LEDs) ('red' 588 nm, B5B-434-TY, 13.5cd, 8°, 20 mA; 'green' 477 nm, RLS-5B475-S; 3-4 cd, 15°, 20mA; 'blue' 415 nm, VL415-5-15; 10-16 mW, 15°, 20 mA; 'ultraviolet, UV' 365 nm, LED365-06Z; 5.5 mW, 4°, 20 mA, Roithner, Germany). LEDs were filtered and combined using FF01-370/36, T450/pxr, ET420/40 m, T400LP, ET480/40x, H560LPXR (AHF/Chroma). The final spectra approximated the peak spectral sensitivity of zebrafish R-, G-, B-, and UV-opsins, respectively, while avoiding the microscope's two detection bands (Figure S3A). LEDs were synchronized with the scan retrace at 500 Hz. Stimulator intensity was calibrated (in photons per second per cone) such that each LED would stimulate its respective zebrafish cone-type with an equal number of photons (~10<sup>5</sup> photons per cone per s). Assuming an effective absorption coefficient of ~0.1, this translates to ~10<sup>4</sup> photoisomerisations per cone per s (R\*), a low photopic regime. We did not attempt to compensate for cross-activation of other cones, and relative LED-versus-opsin cross sections are listed in Figure S3A. Owing to two-photon excitation of photopigments, an additional, steady illumination of ~10<sup>4</sup> R\* was present during the recordings (for detailed discussion, see [3, 80]). For all experiments, the animal was kept at constant illumination for at least 5 s after the laser scanning started before light stimuli were presented. The only stimulus used throughout this work was a "tetrachromatic binary noise" stimulus. Here, each of the 4 LEDs was simultaneously but independently driven in a known binary sequence at 12.8 Hz for 258 s.

### Immunohistochemistry

For the IPL structural analysis, whole fixed larvae (7-8 dpf) were incubated in permeabilisation/blocking buffer (PBS with 0.5% Triton X-100 and 5% normal donkey serum) for at least 10 min followed by 3-5 days incubation at 4°C with primary antibodies (chicken anti-GFP (AbCam, 13970, 1:500), goat anti-ChAT (Chemicon, AB144P, 1:50), rabbit anti-PKC $\alpha$  (Sigma, P4334, 1:100)). Samples were rinsed three times in phosphate buffered saline with 0.5% Triton-X 100 and incubated for another day with secondary antibodies and Hoechst 33342 (1:5000) for nucleus staining in permeabilisation/blocking buffer. Finally, samples were washed in PBS with 0.5% Triton X-100 and mounted in mounting media (VectaShield, Vector, H-1000) for fluorescent imaging. Secondary antibodies used were as follows: Donkey anti-chicken IgG CF488A conjugate (Sigma, 1:500), Donkey anti-rabbit IgG CF568 conjugate (Sigma, 1:500), Donkey anti-goat IgG DyLight650 conjugate (BETHYL, 1:200). For photoreceptors, whole eyes were dissected from the animal at 7-8 dpf and subsequent tissues were subjected to immunohistochemistry as described above. Antibodies used are, a primary antibody: zpr-1 (ZFIN, 1:50), and a secondary antibody: Donkey anti-mouse IgG DyLight649 conjugate (Jackson Immunoresearch laboratories, 1:500). Confocal images were taken on Leica TCS SP8 or Olympus FV1000 using objectives 63x (HC PL APO oil CS2, Leica), 20x (HC PL APO Dry CS2, Leica), 60x (UPLSAPO oil, Olympus) or 20x (UPLSAPO oil, Olympus) at xy: 0.1-0.07 μm/pixel, and z-step: 0.25-0.3 μm for high-resolution images and 0.7-0.5 μm/pixel, and z-step: 2 μm for low magnification images. Images were median-filtered and contrast and brightness were adjusted in Fiji (NIH).

### Photoreceptor densities

Confocal image stacks of whole eyes were converted to spherical max-projection image stacks using custom-written scripts in IGOR pro 6.3 (Wavemetrics). The image plane crossing photoreceptor somata in this spherical projection was used to automatically identify cells using a threshold function in SARFIA [81] running under IGOR Pro. After manual verification and correction in Fiji, photoreceptor positions were projected back onto a 3D hemi-sphere and density was calculated using custom IGOR Pro scripts. Density maps (Figures 2A and 2B) are top-down views of these 3D hemi-spheres. For extracting density profiles linearised against eye position

(Figures 2C and 2D) we computed the mean density in a ring between 112°–145° eccentricity, whose angular center of mass corresponds to 130°. This “3D ring” was chosen as it corresponds to the same sagittal plane as surveyed for inner retinal anatomy and function (Figures 2E and S2).

### The number of neurons in the 7–8 dpf larval zebrafish

Our photoreceptor-labeling experiments (Figure 2) revealed that at 7–8 dpf, a single eye comprises approximately 10,000 photoreceptors (all cones and rods combined). From here, we then estimated HC and BC numbers as ~1,000 and ~25,000, assuming these neuron classes comprise 4 (HC) and 25 (BC) types that each tile the retina with no overlap, with each type on average contacting 30 (HC) and 10 (BC) PRs [56, 82–84]. Finally, there are ~4,000 RGCs in the larval zebrafish eye [85], and from here we assumed that ACs make up at least another 4,000 neurons. This puts the total number of neurons for both eyes added up ~88,000. In comparison to ~85,000–100,000 neurons in the brain excluding the eyes [86], this estimate implies that about half the brain’s neurons are located in the eyes.

## QUANTIFICATION AND STATISTICAL ANALYSES

No statistical methods were used to predetermine sample size.

### Data analysis

Data analysis was performed using IGOR Pro 6.3 (Wavemetrics), Fiji (NIH) and Python 3.5 (Anaconda distribution, scikit-learn 0.18.1, scipy 0.19.0 and pandas 0.20.1).

### Pre-processing and receptive field mapping

Regions of interest (ROIs), corresponding to individual presynaptic terminals of BCs were defined semi-automatically by custom software (D. Velychko, cf [87]). Next, the  $\text{Ca}^{2+}$  traces for each ROI were extracted and de-trended by high-pass filtering above ~0.1 Hz and followed by z-normalization based on the time interval 1–6 s at the beginning of recordings using custom-written routines under IGOR Pro. A stimulus time marker embedded in the recording data served to align the  $\text{Ca}^{2+}$  traces relative to the visual stimulus with a temporal precision of 2 ms. We then mapped linear receptive fields of each ROI by computing the  $\text{Ca}^{2+}$  transient-triggered-average. To this end, we resampled the time-derivative of each trace to match the stimulus-alignment rate of 500 Hz and used thresholding above 0.7 standard deviations relative to the baseline noise to the times  $t_i$  at which Calcium transients occurred. We then computed the  $\text{Ca}^{2+}$  transient-triggered average stimulus, weighting each sample by the steepness of the transient:

$$\mathbf{F}(l, \tau) = \frac{1}{M} \sum_{i=1}^M \dot{\mathbf{c}}(t_i) \mathbf{S}(o, t_i + \tau).$$

Here,  $\mathbf{S}(l, \tau)$  is the stimulus (“LED” and “time”),  $\tau$  is the time lag (ranging from approx. –1,000 to 350 ms) and  $M$  is the number of  $\text{Ca}^{2+}$  events. RFs are shown in z-scores for each LED, normalized to the first 50 ms of the time-lag. To select ROIs with a non-random temporal kernel, we first concatenated all four color kernels to a single vector (X by 1) and computed the standard deviation across this vector. We used all ROIs with a standard deviation of at least two. The precise choice of this quality criterion does not have a major effect on the results.

### Feature extraction and Clustering

For each ROI, we concatenated the kernels for all colors, forming one 2,496-dimensional vector (4 times 649) per ROI. We then denoised this vector by using the reconstruction obtained from projecting it on the first 40 PCA components, capturing ~90% of the variance. We then followed a feature extraction and clustering pipeline described previously [87]. We computed three PCA features on each color channel individually, yielding a total of 12 features. They captured between 70 and 83% of the variance per channel. We fit a Gaussian Mixture Model to the data, optimizing the Bayesian Information Criterion (BIC) for the number of mixture components. The covariance matrix of each cluster was chosen to be diagonal and a regularisation term of  $10^{-6}$  was added to the diagonal. The BIC curve was shallow between 22 and 27 clusters, with a minimum at 26. Spherical covariance matrices or the identical covariance matrix for each cluster yielded higher BIC scores. Full covariance matrices yielded somewhat lower BIC scores with an optimum at a cluster number below 10. In this case, functionally heterogenous clusters were grouped together. This analysis was performed in Python 3.5 using scikit-learn implementations.

### Grouping of clusters into response groups

Each cluster was allocated into one of four response groups ( $n = 25$ ) or discarded ( $n = 1$ ). For each cluster mean and each channel, we first calculated the peak to peak amplitude in z-scores relative to each channels baseline, defined as the first 50 ms of each kernel. If the mean difference of the mode of all amplitudes between the UV and all other channels exceeded 35, that cluster was classified as UV(B) monochromatic ( $C_{6-14}$ ). Similarly, a single cluster with mean mode amplitude below 2 was discarded ( $C_x$ ). Next, we calculated the correlation between all pairs of channels as well as the variance between amplitudes, with the mean between amplitudes normalized to 1. If the mean correlation between all pairs exceeded 0.8 (i.e., similar waveforms) and the variance of amplitudes was below 0.09 (i.e., similar amplitudes), that cluster was classified as achromatic ( $C_{1-5}$ ). Finally, to distinguish remaining chromatic

(C<sub>15-20</sub>) and color opponent clusters (C<sub>21-25</sub>), we also computed the mean of the mode of all correlations. If the mean of correlation equalled the mean of the mode of correlations (i.e., all kernels had the same polarity), that cluster was classified as chromatic. All remaining clusters were classified as color opponent. Following this automatic pre-sorting, we manually reallocated three clusters that were misclassified due to low amplitudes of individual kernels: C<sub>17</sub> and C<sub>20</sub> were moved from color opponent to chromatic as the very low amplitudes of the R-channel led to these clusters' erroneous classification, and C<sub>9</sub> was moved from the chromatic to the UV(B) monochromatic group as this cluster effectively only responded to UV-stimulation but the overall low-amplitudes led its misclassification. Finally, we also moved C<sub>21</sub> from the chromatic to the opponent group. Here, the pronounced time-course difference between UV(B) and RG that leads to a clear opponency in the early kernel period was not picked up by our automatic sorting rules.

#### Histograms against eye position

All histograms against eye position were smoothed using a circular 60° binomial (Gaussian) filter along the x-dimension and IPL depth histograms were in addition smoothed by a 5%-width Gaussian filter across the y-dimension. Moreover, all 2D histograms of both eye position and IPL depth (Figures 4, 5, and 6) were warped to horizontally align the peaks of the major anatomical IPL layers across eye position (Figure 5A, top row). Specifically, the IPL was compressed from the top by 5% at the outward horizon and by 5% from the bottom of the IPL at the forward horizon, where the IPL is thickest (cf. Figure 2K).

#### DATA AND SOFTWARE AVAILABILITY

All 2-photon imaging and natural imaging data are available at <http://www.badenlab.org/resources> and <http://www.retinal-functomics.net>. All other data and code is available upon request.

**Current Biology, Volume 28**

**Supplemental Information**

**Zebrafish Differentially Process Color  
across Visual Space to Match Natural Scenes**

**Maxime J.Y. Zimmermann, Noora E. Nevala, Takeshi Yoshimatsu, Daniel Osorio, Dan-Eric Nilsson, Philipp Berens, and Tom Baden**

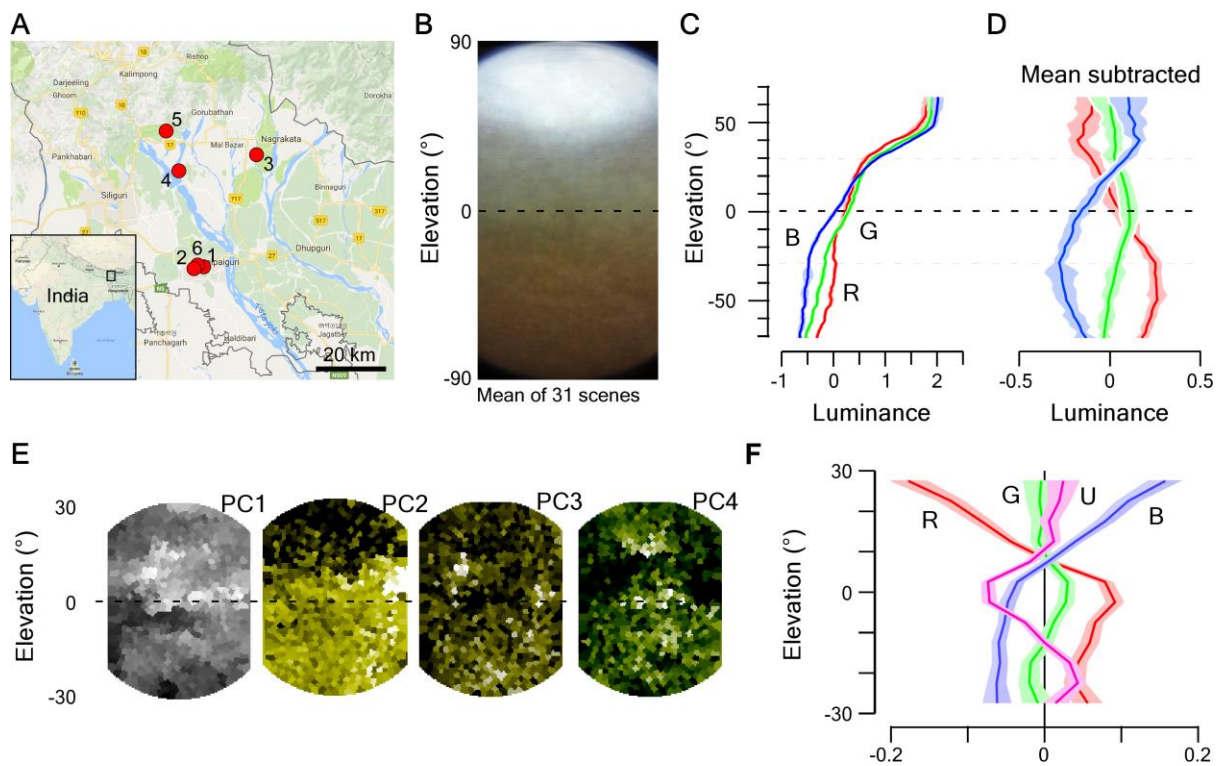


**Figure S1: Distribution of chromatic content in the zebrafish natural visual world.**

**Related to Figure 1.** **A**, Location of field sites visited in West Bengal, India. **B**, Mean of n=31 action camera images and **C**, mean z-normalised brightness of the red, green and blue camera channels across these scenes. **D**, As (C), with mean between all 3 channels subtracted to highlight the differences between the three channels. Errors in C,D in s.e.m. **E**, Principal components 1-4 (left to right) of the hyperspectral example image shown in Figure 1J, (cf. Figure 1B-D). **F**, Achromatic-mean-subtracted mean luminance of the 4 opsin channels from the same scene (like in D). Errors in s.e.m..

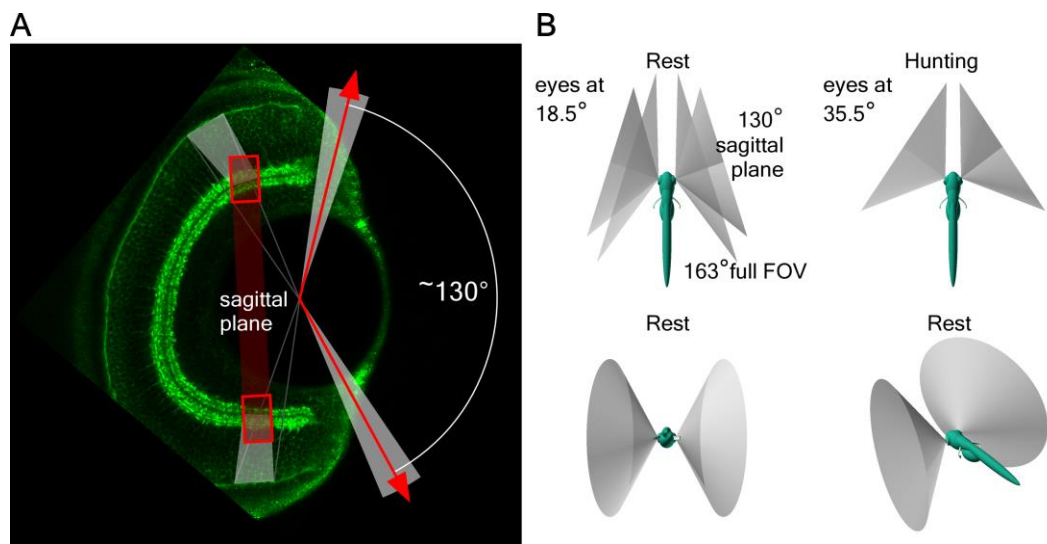


**Figure S2: Anisotropic retinal structure. Related to Figure 2.** **A**, Transverse plane (looking down onto the fish from the top) immunolabelled 7 *dpf* larval zebrafish eye with bipolar cell terminals in green (like Figure 2L) highlights the ~130° visual angle surveyed by the sagittal plane used throughout this work (indicated in red). **B**, 3D illustrations of the field of view covered by this sagittal plane during “rest” (eyes tilted forward ~18.5°) and during prey-capture (“hunting”, eyes at 35.5°) as indicated. In the top left panel, the ~163° full field of view of the eye is indicated in addition to the 130° field surveyed in this work.

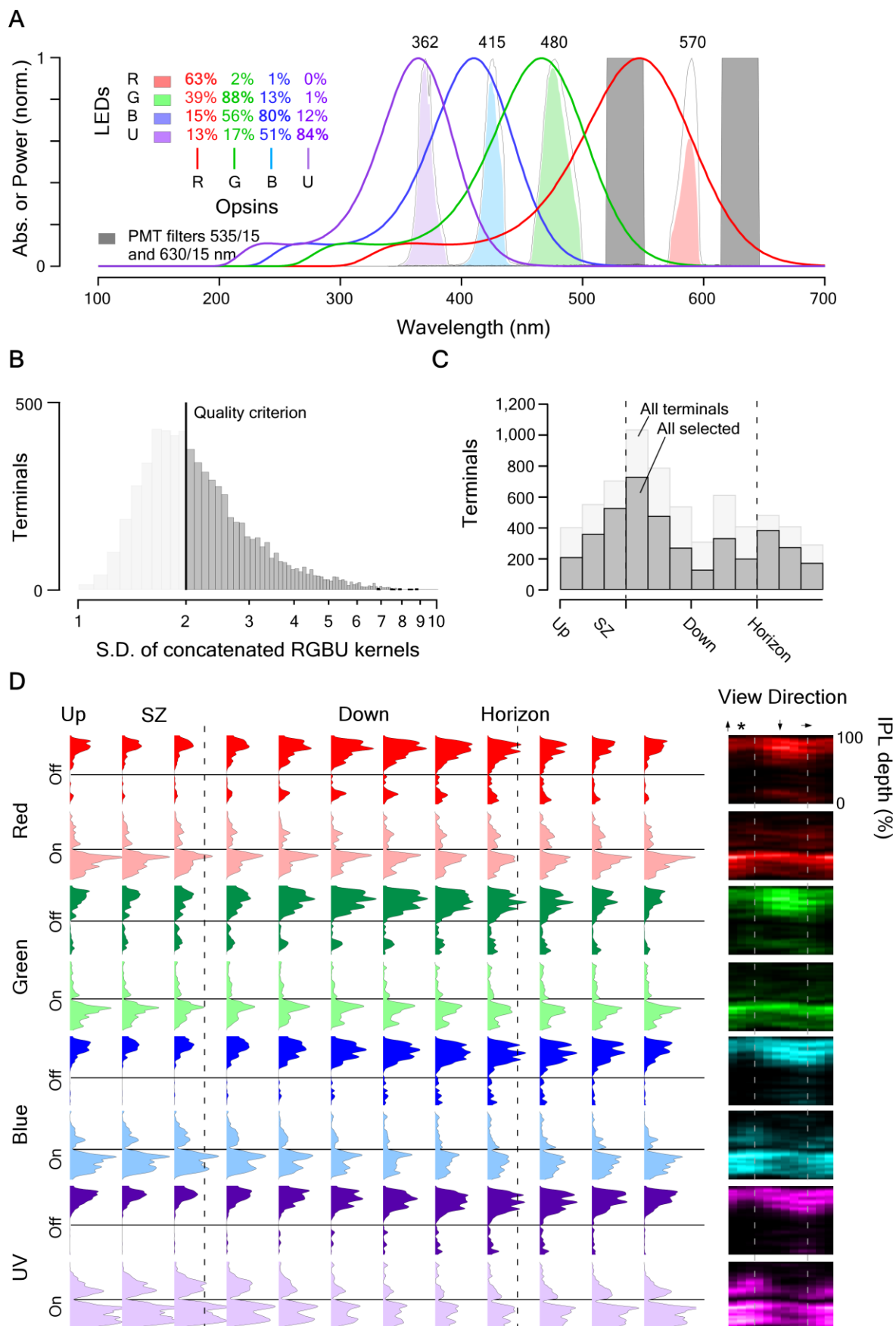


**Figure S3: Surveying inner retinal chromatic responses *in vivo*. Related to Figure 3.** **A**, Cone action spectra (thin lines) plotted on top of effective LED spectra as measured at the sample plane (black lines) and each LED's spectral cross-section with respective target cone in solid colours. Grey boxes indicate the positions of the two detector bands. Cross activation efficiencies between LEDs and each cone action spectrum are listed in the inset. The red-LED's long-wavelength emission spectrum was chosen to limit spectral overlap with the red-fluorescence detection channel. Any loss in excitation efficiency of the red opsin was compensated for by increasing this LED's power accordingly. **B**, Histogram of quality criterion (Methods) for all recorded terminals with cut-off value of 2 z-scores indicated and **C**, distribution of all (light) and selected (dark) terminals across the eye. **D**, Distribution of R, G, B, U Off- and On- responses across the IPL depth (vertical axis) and eye position (horizontal axis) as indicated (cf. Figure 3H-K). The insets to the right show the same data plotted as heatmaps.

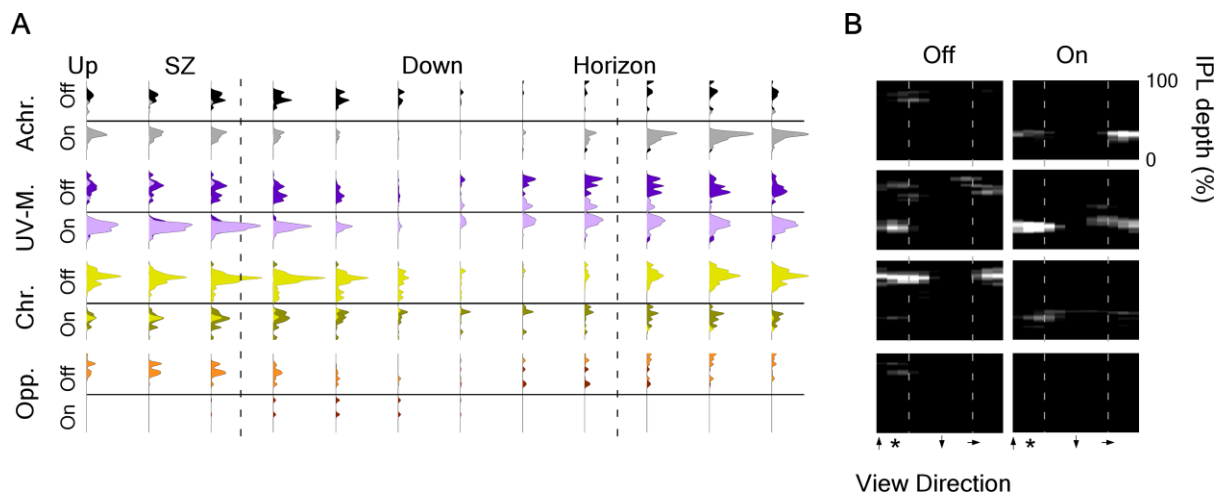


**Figure S4: Distribution of morphologically defined BC-types. Related to Figure 6.** A, Distribution of *xfz43*-positive BC responses split by polarity (Off / On) and allocated major response group plotted against IPL depth (vertical axis) and eye position (horizontal axis). B, Same data as (A), plotted as heatmaps.